

## Small Scale Structure at High Redshift: II. Physical Properties of the C IV Absorbing Clouds<sup>1</sup>

Michael Rauch<sup>2</sup>, Wallace L.W. Sargent<sup>3</sup>, Tom A. Barlow<sup>3</sup>

### ABSTRACT

Keck HIRES spectra with a resolution of 6.6 or 4.3 km s<sup>-1</sup> were obtained of the separate images of three gravitationally lensed QSOs, namely Q0142-0959 A,B (UM 763, A,B) ( $z_{em} = 2.72$ ), Q1104-1804 A,B ( $z_{em} = 2.32$ ), and Q1422+2309 A,C ( $z_{em} = 3.62$ ). The typical separation of the images on the sky is  $\sim 1''$ . The corresponding transverse distances between the lines of sight range from a few tens of kpc at the redshift of the lens to a few pc at the source. We studied the velocity differences and column density differences in C IV doublets in each QSO, including single, isolated doublets, complex clumps of doublets and sub-clumps. Unlike the low ionization gas clouds typical of the interstellar gas in the Galaxy or damped Ly $\alpha$  galaxies, the spatial density distribution of CIV absorbing gas clouds turns out to be mostly featureless on scales up to a few hundred parsecs, with column density differences rising to 50% or more over separations beyond a few kpc. Similarly, velocity shear becomes detectable only over distances larger than a few hundred pc, rising to  $\sim 70$  kms<sup>-1</sup> at a few kpc. The absorption systems become more coherent with decreasing redshift distance to the background QSO; this finding confirms that all 3 QSOs used are indeed lensed, as opposed to being genuine QSO pairs.

The amount of turbulence in CIV gas along and across each line of sight was measured, and a crude estimate of the energy input rate obtained. The energy transmitted to the gas is substantially less than in present day star-forming regions, and the gas is less turbulent on a given spatial

---

<sup>1</sup>The observations were made at the W.M. Keck Observatory which is operated as a scientific partnership between the California Institute of Technology and the University of California; it was made possible by the generous support of the W.M. Keck Foundation.

<sup>2</sup>Carnegie Observatories, 813 Santa Barbara Street, Pasadena, CA 91101, USA

<sup>3</sup>Astronomy Department, California Institute of Technology, Pasadena, CA 91125, USA

scale than, e.g., local HII regions. The quiescence of CIV clouds, taken with their probable low density, imply that these objects are not internal to galaxies. The C IV absorbers could be gas expelled recently to large radii and raining back onto its parent galaxy, or pre-enriched gas from an earlier (population III ?) episode of star formation, falling into the nearest mass concentration. However, while the metals in the gas may have been formed at higher redshifts ( $z > 5?$ ), the residual turbulence in the clouds and the minimum coherence length measured here imply that the gas was stirred more recently, possibly by star formation events recurring on a timescale on the order of  $10^7 - 10^8$  years.

*Subject headings:* intergalactic medium — cosmology: observations — galaxies: high redshift, abundances — quasars: absorption lines — gravitational lensing — quasars: individual (UM673, HE 1104-1805, Q1422+231)

## 1. Introduction

In the second paper of a series on small scale structure in the baryon distribution at high redshift, we study metal-enriched gas as seen in absorption by CIV against multiple images of gravitationally lensed QSOs. Paper I (Rauch, Sargent and Barlow 1999) dealt with a particular low ionization metal system at redshift 3.58, which showed density and velocity structure on scales of a few tens of parsecs, consistent with a gas outflow on a very small (stellar) scale, possibly a supernova remnant. The density, metallicity, and kinematics of the absorption system resembled the ISM in our galaxy. However, such strong, low ionization (ISM) regions of interstellar gas are relatively rarely traversed by random QSO lines of sight. High ionization CIV absorption systems outnumber them by about 2 orders of magnitude (down to column density limits of  $N(\text{CIV}) \sim \text{a few} \times 10^{12} \text{cm}^{-2}$ ). In the present paper we turn our attention to the statistical properties of the high ionization CIV gas phase.

The CIV ( $\lambda\lambda 1549, 1550 \text{ \AA}$ ) doublet in absorption is the most commonly observed signature of metal enriched gas at high redshift. Most of the CIV systems seen belong to highly ionized gas, optically thin at the HI Lyman Limit. Line widths are consistent with a photoionized gas ( $T \sim \text{a few} \times 10^4 \text{ K}$ ) with about equal contributions from thermal and non-thermal motion (Rauch et al. 1996). At redshift  $z = 3$ , densities of gas with detectable CIV absorption appear to range between a few times the mean

density of the universe to values somewhat below those of a virialized galactic halo (Rauch, Haehnelt & Steinmetz 1997; assuming photoionization by a standard QSO UV background). The CIV absorption components are highly clustered on scales of several hundred  $\text{kms}^{-1}$  (Sargent et al 1979; Steidel 1990; Petitjean & Bergeron 1994).

The stronger CIV absorption systems studied by several surveys during the past two decades have often been interpreted as gas clouds orbiting in hypothetical, gaseous galactic halos (e.g., Sargent et al. 1979; Bergeron & Boissé 1991; Steidel 1993; Petitjean & Bergeron 1994; Mo & Miralda-Escudé 1996). The physical origin of the CIV clouds themselves and their relation (if any) to known present-day Galactic environments is not clear. They may conceivably be related to proto-globular clusters (e.g., Fall & Rees 1985; Kang et al 1990; Peng & Weisheit 1991), but it is also possible that they are caused by galactic winds (e.g., Fransson & Epstein 1982; Wang 1995), or tidal debris (Wang 1993; Morris & Van den Bergh 1994).

Recent work with the Keck HIRES instrument (Cowie et al. 1995; Tytler et al. 1995; Womble et al 1996; Cowie & Songaila 1998) has detected CIV absorption even in the diffuse, low density gas clouds giving rise to the  $\text{Ly}\alpha$  forest. These structures turned out to already being metal-polluted at high redshift (at the 50% level for gas with a neutral hydrogen column density  $> 10^{14.5} \text{ cm}^{-2}$ ), reaching a median metallicity  $Z \sim 10^{-2.5} Z_{\odot}$  by redshift  $z \sim 3$ , albeit with a substantial scatter of about a magnitude. There is evidence for some metal enrichment at even lower column densities (Ellison et al 2000, Schaye et al 2000). The high rate of incidence together with the large velocity widths and inferred low gas densities of many CIV systems argue for a more complex origin of the absorbers than the simple picture of gas clouds in a hydrostatically supported halo can provide. Continued infall or outflows of metal enriched gas beyond the virial radius of high redshift galaxies may be important.

A CDM -based scenario where CIV absorption arises in metal-enriched gas accreting onto and shocked by forming galaxies has been discussed by Rauch, Haehnelt, und Steinmetz (1997). In this model CIV systems at high redshift correspond to groups of protogalactic clumps prior to merging, which are the building blocks of future normal galaxies. In this interpretation, the large velocity widths of CIV absorption systems are a natural consequence of mergers between two or more clumps or chance alignments of filamentary groups of such objects along our line of sight. The basic limitation of the original version of this model is its reliance on gravitational instability as the sole mechanism for structure formation. Stellar 'feedback' (in

the form of discrete sources of ionization, momentum and energy input, and stellar metal production) is capable of strongly modifying the gas distribution locally, e.g., it may produce outflows locally superseding the general infalling motion. We expect the observed properties of the CIV gas– its ionization state, kinematics and small scale texture– to reveal its relation to the stellar outflows on one hand and the intergalactic baryonic reservoir on the other. In particular we would like to determine the density fluctuations and characteristic sizes of the high ionization (CIV) gas clouds and the magnitude of the internal velocity gradients as measured in projection. As in paper I we employ observations of absorption lines in spectra of the separate images of gravitationally lensed QSOs to obtain these constraints.

Earlier lensing studies have produced important constraints on the size scales of the intergalactic gas clouds giving rise to the Ly $\alpha$  forest. Observations of lensed QSOs (Foltz et al. 1983; Smette et al. 1993,1995), taken together with similar constraints from the observation of QSO pairs at larger separations (e.g., Sargent et al. 1982; Shaver & Robertson 1983; Bechtold et al. 1994; Dinshaw et al. 1994,1995; Fang et al. 1996, Petry et al 1998) indicate the presence of large gaseous bodies, coherent over several hundred kiloparsecs. In contrast, the objects responsible for metal absorption systems (especially damped Ly $\alpha$  systems) appear to have sizes up to a few tens of kpc and smaller differences in their equivalent widths across the lines of sight (Young et al. 1981; Smette et al. 1993,1995; Crofts et al. 1994; Bechtold & Yee 1995; Zuo et al. 1997; Michalitsianos et al. 1997; Monier, Turnshek & Lupie 1998; Lopez et al 1997; Petitjean et al 2000).

Before the advent of the Keck telescope observations of absorption in multiple lines of sight at high redshift have been very difficult and were limited to a resolution too low to make strong inferences about the structure of metal systems. Using the Keck High REsolution Spectrograph (HIRES; Vogt et al. 1994) we have begun a survey of all gravitationally lensed QSOs bright enough to be observed with HIRES ( $m < 19$ ) and visible from Hawaii, which have image separations wide enough to be separated in good seeing ( $> 1''$ ). In this paper we present the results of our observations of three QSOs– Q0142-0959 A,B (UM 763, A,B) ( $z_{em} = 2.72$ ), Q1104-1804 A,B ( $z_{em} = 2.32$ ), and Q1422+2309 A,C ( $z_{em} = 3.62$ ). A convenient summary of the observed properties of each QSO may be found on the CASTLES web site (<http://cfa-www.harvard.edu/castles/>). Details of the observations and data analysis are given in section 2, the results are discussed in section 3 and the conclusions are summarised in section 4.

## 2. Observations and Data Analysis

The three brightest QSOs in our sample, with redshifts ( $z > 1.6$ ) suitable for the study of CIV absorption are UM673 (Surdej et al 1988), HE104-1805 (Wisotzki et al 1993), and Q1422+2309 (Patnaik et al 1992). The spectra cover the wavelength ranges  $\lambda\lambda 3608-6094$  (UM 273 and HE1104-1805) and  $\lambda\lambda 4832-7348$  (Q1422+2309). For UM673 and HE1104-1805 we used a  $7'' \times 0.86''$  decker, giving a spectral resolution of  $6.6 \text{ km s}^{-1}$  (FWHM). For Q1422+231, because of the small separation of the images ( $1.3''$ ), a narrower slit ( $7'' \times 0.574''$ ) was used to reduce mutual contamination of the spectra. All spectra were taken with the red crossdisperser, which was the only one available when the observations started (1996). The individual images were put separately on the slit to facilitate sky-background subtraction and offslit guiding. Guiding was done mostly by hand because the automatic guider was found to be unreliable for this particularly demanding type of observation. The slit was aligned as closely as possible to the parallactic angle, consistent with minimizing the spillover from the image not being observed.

The A (B) image of UM673 was exposed for 13500s (33100s), the A (B) image of HE1104-1805 for 19300s (51200s), and the A (C) image of Q1422+2309 for 19600s (33200s), respectively. The A and B images of Q1422+2309 were judged to be too close together for reliable observation of the B image. We note that the main observational difficulty is to obtain satisfactory spectra of the fainter image of each pair. The extra exposure times listed above for the fainter images do not completely compensate for the differences in brightness of the two images.

The data were reduced using the HIRES data reduction package MAKEE written by one of us (TAB; see Barlow & Sargent 1996). For each QSO the spectra from the different echelle orders of each image were combined. The continua redward of the Ly $\alpha$  emission line of both images were normalized by using polynomial fits to spectral regions apparently free of absorption lines.

Two examples of strong CIV systems toward UM673 are shown in Fig. ???. The systems are at redshifts  $z_{abs} = 1.94$  (top; separation between the lines of sight:  $1.7 h^{-1} \text{ kpc}$ ) and  $2.355$  (bottom; separation between the lines of sight:  $0.63 h^{-1} \text{ kpc}$ ). Both objects show remarkably large velocity extents ( $510$  and  $260 \text{ km s}^{-1}$ ) along the line of sight. In the upper image the first group of absorption lines ( $0 < v < 250 \text{ km s}^{-1}$  on the arbitrary velocity scale) appears to be affected by a coherent velocity shear across the lines of sight. In contrast, the sharp, 'single' absorption doublet

near  $450 \text{ km s}^{-1}$  is at nearly the same position in both images. Such an absorption pattern could conceivably arise during the merger of two galaxies which happen to be moving approximately along our line of sight. The large velocity extent along the line of sight may be caused by the infalling motion, and rotation in the first object may be causing the velocity shear in the lower redshift clump. In the bottom spectrum ( $z_{abs} = 2.355$ ), the differences are somewhat less dramatic, and may possibly be explained by fluctuations in the gas density internal to a single galaxy.

To quantify line of sight differences in the CIV absorption systems we proceeded as follows: For the further analysis, only the regions of the spectra longward of Ly $\alpha$  emission were used. CIV systems were identified. It is hard to estimate an overall completeness limit, since the S/N ratio varies along the spectra, and Q1422+231 had a significantly higher S/N ratio than the other two QSOs. Trials indicate that any (unblended) CIV doublet with a Doppler parameter of order  $7 \text{ km s}^{-1}$  and with  $N(\text{CIV}) \geq 5 \times 10^{12} \text{ cm}^{-2}$  would have been seen in most of the spectra of the three objects.

The CIV lines were modelled with Voigt profiles, using the  $\chi^2$  minimization fitting program VPFIT (Carswell et al 1992). The two lines of the CIV ( $\lambda\lambda 1548, 1550 \text{ \AA}$ ) doublet were profile-fitted simultaneously with as few components as necessary to achieve a statistically acceptable reduced  $\chi^2$  value (e.g., Carswell et al 1991). Absorption line interlopers from other, unrelated metal transitions were also fitted. Then a velocity window was run over the CIV line list to identify absorption *complexes*. Two absorption components were defined to belong to the same complex, when they were less than  $1000 \text{ km s}^{-1}$  apart in their rest frame. Then, stretches of the spectrum with length  $1000 \text{ km s}^{-1}$ , each containing one CIV system or complex, were reconstructed from the line lists. These 'noise-free' mini-spectra were used for further analysis. They are shown in figs. 2-5 for Q1422+231, and figs. 6 and 7, for HE1104-1805 and UM673, respectively.

We next describe the velocity and column density structure of these systems, and the dependence of these physical parameters on the line of sight separation. Then, we attempt to measure the typical size of the absorbers.

## 2.1. Complexes, subclumps, and single components

As indicated in the above discussion there may be reason for subdividing the observed absorption pattern into smaller units. To make further progress we have attempted to crudely classify absorption features and substructure within a given absorption complex by eye. Once we have established a correspondence between features seen in multiple lines of sight, we can measure the gradients in velocity and column density across the lines of sight.

We proceed such that groups and substructures of absorption systems thought to correspond to each other are selected interactively in both lines of sight. The properties (total column density; column density-weighted velocity; total velocity width) are then computed for each feature in both lines of sight. We fairly arbitrarily define three classes of absorption pattern, which we compare separately:

- (1) the whole absorption system– (“Complexes”)
- (2) distinctly different groups of components within a system– (“Subclumps”)
- (3) single absorption lines – (“Components”)

The meaning of class (1) and (3) is immediately clear, but class (2) is more vaguely defined as a close subgroup within an absorption complex – implying that there are additional components at larger separation than the typical intercomponent distance of the subgroup. In other words, the transmitted flux level *between* clumps is substantially higher than within them. This classification is illustrated in figs. 2 – 7, and in tables 1-3 . The figures show all CIV systems detected in the three QSO spectra, with the spectrum of the A image on top and that of the B (or C) image at the bottom. Redshifts are given in the RHS bottom corner. The velocity range of each set of components as selected by eye using the criteria given above is indicated by a dotted line, bounded by two larger dots. Regions with the same numbers in different images are meant to correspond to each other. Most of the time the correspondence in the two spectra between the larger complexes is unambiguous and the velocity position and width of the window is very similar in both images. Occasionally, especially in the case of single components, it is unclear whether we are really seeing the same structure in the two spectra; this must be kept in mind for later interpretation. The numbers within a given absorption system correspond to the entries in tables 1-3. The tables give for each system first the redshift  $z_{abs}$

and transverse separation  $r$  between the lines of sight, followed by as many entries as there are velocity regions defined. The parameters in each line are: the integrated column densities  $N_A$ ,  $N_B$  (for the A and B images), the logarithmic column density difference  $\Delta \log N$  between the two lines of sight, the difference between the column density weighted mean velocities,  $\overline{v_A} - \overline{v_B}$ , and the total bulk motion velocity widths  $\Delta v_A$ ,  $\Delta v_B$  of each structure. If the feature can be fitted by a single Voigt profile, no velocity width is given. The last column in tables 1 - 3 consists of three subcolumns, giving the class of each subgroup in the window. For example 1 0 0 means that the window includes the whole absorption system (class 1), whereas 1 0 3 would imply that the system belongs to class 1 and 3 simultaneously (i.e., it the whole system consists of a single component). The combination 0 2 0 denotes a subgroup of several components.

The results of these measurements are illustrated in Figs. 8 – 13. Because the sample is very small we refrain from imposing a uniform selection according to the signal-to-noise level or minimum column density, and show all the data in one plot for all the systems detected.

## 2.2. Differences in column density as a function of separation between the lines of sight

We can define the 'size' or 'coherence length' of a gas cloud as the distance over which there are significant changes in the physical parameters. The quantities most straightforward to measure are changes in the column density and in the projected velocity between the lines of sight.

Fig. 8 shows the fractional difference between the CIV column densities,  $(N_A - N_B)/\max(N_A, N_B)$ , versus the transverse separations between the lines of sight  $A$  and  $B$ , on a logarithmic scale. The fractional difference of any absorption system obviously lies between 0 (system identical in both lines of sight) and 1 (system only present in one line of sight, not in the other). The information is given separately for all three categories as defined above, namely absorption complexes (large circles), subclumps (small circles), and single components (dots). The two arrows show upper limits for two complexes where the absorption system was present only in one line of sight but not in the other. The beam separation is computed assuming  $q_0 = 0.5$  and the following lens redshifts: UM673:  $z_{lens}=0.493$  (Surdej et al 1988); Q1422+231:

$z_{lens}=0.338$  (Kundic et al 1997); HE1104-1805:  $z_{lens}= 0.73$  (Wisotzki et al. 1998). On the basis of a time-delay estimate the latter authors have argued that the redshift of the lensing galaxy is not as high as originally assumed ( $z_{lens}=1.32$  or  $1.66$ , the location of two candidate absorption systems in the line of sight) but may coincide with a system at  $z_{lens} = 0.73$ . (After the present paper was completed Lidman et al (2001) have detected a  $z=0.73$  galaxy in emission and presented additional arguments that this is the lensing object). The beam separation for an absorption system at redshift  $z = 2$  increases by a dramatic factor 5 when the lens redshift is moved from  $0.73$  to  $1.66$ , so knowing the precise lens redshift is crucial for quantitative inferences. For comparison, we show in fig.9 the same plot with the lens redshift of HE1104-1805 set to  $z = 1.32$ . The lens redshift of UM673 is also somewhat uncertain (there are three MgII absorption systems near  $z \sim 0.5$ , one of which ( $z_{abs} = 0.56358$ ) is stronger and more symmetric in both lines of sight than the absorption pattern caused by the presumed lens).

### 2.2.1. Testing the lensing hypothesis

Although the scatter in figs. 8 and 9 is quite large (which is partly due to the pixel noise in the data - a problem for weak systems close to the detection threshold), one of the most basic trends expected is indeed observed: the larger the beam separation, the greater is the column density difference between corresponding absorption systems. This trend shows that the three QSOs are indeed gravitationally lensed and do not consist of pairs of individual QSOs. In the lensed case, for absorption redshifts  $z_{lens} < z_{abs} < z_{QSO}$ , the beam separation is a rapidly decreasing function of redshift, whereas for genuine QSO pairs the beam separation increases with redshift and levels off or converges only weakly at higher redshifts, depending on the cosmological model. Plots of this sort should provide a useful test for checking the lens-versus-pair hypothesis for multiple QSO images. If, in the future, a sufficient number of lensed QSOs can be observed to establish good limits on the CIV absorption sizes, we may even be able to reconstruct the lens redshifts of individual lensed QSOs by matching the degree of difference between absorption systems along their lines of sight.

### 2.2.2. A minimum size for CIV 'clouds'

With the exception of the absorption complex at  $z=2.298$  in HE1104-1805 (which lies at separation 60 pc for a lens redshift  $z=0.73$  (fig. 8), but at 170 pc for a lens redshift  $z=1.32$  (fig.9), there is very little difference between the column densities for line of sight separations below about 300 pc (Fig.8). For separations larger than that, the differences increase dramatically and reach 50% just below 1 kpc. *Apparently, the spatial distribution of highly ionized CIV gas is mostly featureless on scales below  $\sim 300pc$ .* At the same time, detectable CIV absorption extends over at least several kpc. These result have important consequences for the nature of CIV absorbers which we will explore further below. Fig.10 and 11 give the analogous plots for *absolute* differences in column density.

### 2.3. Relative differences between velocities along the line of sight as a function of separation

Fig. 12 shows the velocity 'shear' as a function of beam separation. The shear or velocity difference  $\Delta v$  between the lines of sight is defined as the difference between the column density weighted velocities,  $\Delta v = \overline{v_A} - \overline{v_B}$ , as seen in the two spectra. The shear slowly rises up to a transverse separation 200-300 pc, beyond which it increases rapidly to  $\sim 60 - 70\text{kms}^{-1}$ , at several kpc. Such values are not unexpected for clouds which partake in the velocity dispersion even of a dwarf galaxy. However, the values should be taken as upper limits, since we know from the results in the previous paragraph that the column densities also have a coherence length on a similar scale. Because of the column density weighting, we may partly confuse column density differences with velocity differences.

### 2.4. The relative differences between velocities along the line of sight as a function of the column density

In fig.13  $\Delta v$  is plotted versus the CIV column density of the system. The observed increase of  $\Delta v$  with  $N(\text{CIV})$  probably implies that the highest density gas experiences the largest velocity dispersion and that the gas is more quiescent where the column density is low.

## 2.5. A lower limit on the overall size of CIV systems

A crude estimate of the total sizes of CIV complexes,  $L_{tot}$ , based on the sizes of individual CIV components can be made as follows:

Multiplying the scale  $r_{1/2}$  over which the individual absorption components change by 50% in column density, say,  $r_{1/2} \sim 300$  pc, by a factor 4 we get an estimate of the minimum size (2 FWHM) of a cloud giving rise to a single CIV component. Then the full CIV complex must be at least as extended along the line of sight as indicated by the number of components  $N_c$  times the size of each component, i.e.,

$$L(tot) \sim 1.2N_c f^{-1} \left( \frac{r_{1/2}}{300\text{pc}} \right) \text{kpc}, \quad (1)$$

where  $f$  is the filling factor of the CIV system for individual clouds. For example, a CIV system with 5 individual components with basically no intercloud space ( $f \approx 1$ ) would imply a size of 6 kpc along the line of sight. If CIV clouds form in situ (i.e., the material ending up in the clouds at density  $\rho_c$  was derived from their immediate surroundings (at original density  $\bar{\rho}$ ) then the formation of the cloud produces an intercloud space such that  $f^{-1} = \rho_c/\bar{\rho}$ . Clouds with an overdensity  $\rho_c/\bar{\rho} = 10$  with respect to the background medium would then have a filling factor  $f = 1/10$  and, according to the above equation, the CIV system would have a typical size of 60 kpc.

## 2.6. Maximum likelihood size estimates for CIV complexes

We use a maximum likelihood method to obtain a parametric estimate of the column density gradients in the plane of the sky given the column densities for a number of systems in both lines of sight or the column density in one and an upper limit in the other line of sight. This is a generalization of the standard technique for estimating the sizes of absorption systems from the numbers of “hits” and “misses” (McGill 1990). A similar approach has been discussed by Smette et al. (1995) to derive lower limits to Ly $\alpha$  cloud diameters. Here we can directly operate with actual column density measurements, or with the upper limits in cases where a system was detected only in one of the two lines of sight. Each absorption system yields only one pair of column density measurements, but if we make the (doubtful) assumption that all clouds are identical, taking one measurement for many systems is equivalent to making many measurements of a single system.

For those systems with definite column densities in both lines of sight we compute the conditional probability density  $p(N_B|N_A, \Delta r)$ , of measuring a column density  $N_B$  in a given system in line of sight B, given a column density  $N_A$  in line of sight A and given a transverse separation  $\Delta r$  between the lines of sight. The probability follows from simple geometric arguments if one assumes that all absorbers possess spherical symmetry and have identical column density profiles, with a semi-definite density gradient,  $dN/dr < 0$  (the assumed situation is illustrated in fig.14). Then, the impact parameter  $r_A$  of line of sight A from the center of an absorbing clump is related to the impact parameter  $r_B$  of line of sight B, the line of sight transverse separation  $\Delta r$ , and the angle  $\phi$  between  $r_A$  and  $\Delta r$  simply by the cosine law

$$r_B^2 = r_A^2 + (\Delta r)^2 - 2r_A\Delta r \cos \phi. \quad (2)$$

A uniform random distribution in  $\phi$  (given fixed  $r_A$  and  $\Delta r$ ) then generates the conditional probability in  $r_B$  and thus in  $N_B$

$$p(N_B|N_A, \Delta r)dN_B = \frac{-r(N_B)}{\pi r(N_A)\Delta r} \frac{dN_B}{\sqrt{1 - \left(\frac{(\Delta r)^2 + r(N_A)^2 - r(N_B)^2}{2r(N_A)\Delta r}\right)^2}} \frac{dr}{dN}(N_B), \quad (3)$$

where the functions  $r(N)$  and  $(dr/dN)(N)$  are derived from a simple model. Here we adopt a Gaussian column density profile,

$$N = N_0 \exp\left(-\frac{1}{2} \left(\frac{r}{r_0}\right)^2\right), \quad (4)$$

where the central column density  $N_0$  and the Gaussian width  $r_0$  are the desired parameters of the model. This parameterization was chosen merely because it is well behaved at the origin, and because its inverse and first derivative are easy to calculate analytically. The few data points and lack of our knowledge about the detailed cloud physics does not appear to justify more sophisticated modelling. It is important, though, to keep in mind that the actual column density distribution may be neither spherically symmetric, or even similar from absorber to absorber. Nor may the column density be close to the values computed from the model in column density ranges where there were few data points to start with, and which consequently are not well constrained. Most importantly, the assumption of a monotonic radius-column density relation may be wrong, and we may be measuring a typical spatial fluctuation scale rather than the width of a coherent object. With these cautionary remarks we

proceed to derive the parameters  $N_0$  and  $r_0$  from a maximum likelihood method, minimizing

$$\ln L = \sum_{j=1}^J \ln p_j + \sum_{j=J+1}^{J_{max}} \ln \int_0^{N_{<}} p_j dN_B. \quad (5)$$

Here

$$p_j = p(N_B(j)|N_A(j), \Delta r(j), N_0, r_0) \quad (6)$$

is the conditional probability, now written as a function of the model parameters  $N_0$  and  $r_0$ , and the sum over the integrals from  $J + 1$  to  $J_{max}$  accounts for those cases where one measurement gives only an upper limit  $N_{<}$  on the column density  $N_B$  (Avni et al 1980). The program was implemented using the minimization routine AMOEBA (Press et. al 1986), and it was tested with random pairs of data points drawn from the said Gaussian model. It was run on those 31 absorption complexes for which at least one line of sight had a CIV absorption system stronger than  $3 \times 10^{12} \text{cm}^{-2}$ . Unfortunately, it was not always possible to get universal convergence (= results independent of the initial values). Likely reasons are the smallness of the sample, and the failure of the simple model. By varying the initial conditions in most cases convergence to values near  $r_0=3$  kpc,  $N_0=5 \times 10^{14} \text{cm}^{-2}$  was obtained, but sometimes  $r_0$  was off by a factor of several. Running the same test on the 27 groups of ‘single components’ (as defined above) the best values were  $r_0=19$  kpc,  $N_0 = 10^{15} \text{cm}^{-2}$ , which gives an idea of the large uncertainties involved. Thus, the technique clearly confirms what we are already have seen by eye - structures in the absorbing gas with a coherence length at least on the order of kiloparsecs - but currently the samples are not adequate to justify more sophisticated analyses. Moreover, lines of sight with larger separation are needed since it appears that the largest cloud sizes have not been sampled by the present dataset.

### 3. Energy input and turbulence

We have derived size estimates for the high ionization gas clouds and measured the degree of decoherence between the projected line of sight velocities across the sky. Combining these results with other findings about the CIV absorbers, we are now in a position to impose constraints on the physical state and origin of the gas, and

to compare the findings with the properties of other, previously known galactic or extragalactic astrophysical environments.

The degree to which gas on a given spatial scale has been stirred by recent stellar processes should give us an idea of any recent star formation activity (winds, SN explosions, ionization fronts). From the data described above it is possible, in a crude way, to measure the turbulence in the CIV gas as a function of spatial scale. Then some basic ideas about astrophysical turbulence (e.g. Chandrasekhar 1949 ; von Hoerner 1951; Kaplan & Pikelner 1970) can be used to estimate the approximate rate of mechanical energy input  $\epsilon_0$  into the gas.

### 3.1. Turbulence deduced from velocity differences between the lines of sight

Most often, astrophysical turbulence has been discussed in connection with the Kolmogorov theory. Here kinetic energy is injected at a rate  $\epsilon_0$  into the gas on a certain scale determined by the geometry and dynamics of the underlying energy source. For fully developed turbulence, the energy propagates with a constant energy transfer rate  $\epsilon \approx \epsilon_0$  through eddies of ever smaller size, until viscosity transforms it into heat. The usual dimensional analysis leads to a relation between the energy transfer rate  $\epsilon$  [in units of  $\text{ergs g}^{-1} \text{s}^{-1}$ , or  $\text{cm}^2 \text{s}^{-3}$ ], and the RMS velocity  $v_s$  between points with spatial separation  $s$ ,

$$\epsilon \sim \frac{v_s^3}{s}. \quad (7)$$

The customarily used structural function

$$B(s) \approx \overline{[v(s') - v(s'')]^2} \simeq \overline{v_s^2} \approx (\epsilon s)^{2/3} \quad (8)$$

(e.g., Kaplan & Pikelner 1970) can be measured from the pairs of column density weighted, line of sight velocities, as a function of projected beam separation. Here the average is taken over all points  $s'$  and  $s''$  with separation  $s$ .

For the CIV gas the quantities  $v_s$  and the projected separation can be read from tables 1 - 3, and the energy transfer rate may be computed and compared with measurements from other known astrophysical environments.

At this point it is worth remembering that the *observed* quantity  $r$  is the transverse separation between two points in two lines of sight, i.e., the distance between

the points projected onto the plane of the sky; we do not know the true separation  $s = \sqrt{s_{\parallel}^2 + r^2}$ . Thus we are not really measuring  $\overline{[v(s') - v(s'')]^2}$  but  $\overline{[v(r') - v(r'')]^2}$ . The relation between projected separation  $s_{\perp}$  and true separation  $s$  depends on the spatial distribution of the clouds and complicates the measurement of the structural function (von Hoerner 1951; Münch 1958; Scalo 1984), leading to an observational underestimate of the true value of  $B(s)$  on scales where  $r \ll s_{\parallel}$ , i.e., when the transverse scales observed are much smaller than the extent of the CIV clouds along the line of sight. This is almost certainly the case for part of our measurements, since beam separations less than a few hundred pc are smaller than the coherence length of individual CIV clouds. Thus we would not expect to observe a Kolmogorov law (a  $B(r) \propto r^{2/3}$  relation) on small scales even if the spectrum of turbulence conforms to it (i.e.,  $B(s) \propto s^{2/3}$ ).

Keeping this complication in mind, we proceed to plot the *observed* structural function  $B_{obs}(r) = \overline{[v(r') - v(r'')]^2}$  for our sample of CIV systems as a function of the transverse beam separation  $r$  in Fig.15. The plot is based on the same data points as listed in tables 1 - 3. However, now the symbols no longer refer to individual CIV systems but give the mean values after the data points have been collected into three logarithmic bins ranging from 10 pc to 100 pc, 100 pc to 1 kpc, and 1 kpc to 10 kpc. For illustrative purposes the dashed line shows a Kolmogorov spectrum ( $\log B(r) = 2/3 \log r + 2/3 \log \epsilon$ ), normalized such that the energy input is  $\epsilon = 10^{-3} \text{cm}^2 \text{s}^{-3}$ . The expected trend for  $B(r)$  to increase with  $r$  is observed, but the agreement with a single power law of slope 2/3 is not overwhelming. There appears to be a tendency for the CIV complexes (large circle symbols) to be more turbulent at the largest separations (or less turbulent at the smallest separations - we do not know the correct normalization a priori) than our naive application of the Kolmogorov assumptions would lead us to expect. This would not be surprising if the velocity differences between the absorption systems on the largest scales are due to a different source of velocity shear. For instance, in a simple hierarchical scenario for galaxy formation, the largest velocity widths of CIV complexes are contributed by the gravitational motions of separate protogalaxies, rather than by turbulent motion on intragalactic scales (Rauch, Haehnelt & Steinmetz 1997). Moreover, the underlying assumptions of the Kolmogorov process (incompressible, subsonic gas, no magnetic fields) may be violated by the CIV gas. However, let us assume that there is at least some overlap between the spatial scales covered by our sample of CIV systems and the ‘inertial’ range of scales where the energy transfer rate is indicative of the original

energy input. Then, judging from the departures of the data points from a straight line (fig.15) it appears that we are not making an error larger than (at most) an order of magnitude in using the y-intersect of the plot in fig. 15 as a crude estimate of the energy input rate  $\epsilon_0$ . Taking values  $B(r) = 100 \text{ km}^2\text{s}^{-2}$ ,  $r = 300 \text{ pc}$  as reference values (the midpoint of the power law in fig. 15), the energy transfer rate is

$$\epsilon \sim 10^{-3} \text{ cm}^2 \text{ s}^{-3}. \quad (9)$$

This is considerably less than values measured for the Orion nebula, where  $\epsilon \sim 0.1 - 1 \text{ cm}^2\text{s}^{-3}$  (e.g. Kaplan & Pikelner 1970), but it is comparable to the global rate of energy input into the ISM of our Galaxy.<sup>4</sup>

### 3.2. Turbulence as measured along the line of sight

Absorption line profiles can also be used to directly probe the turbulent velocity *along* the line of sight, if the line profiles of two ions of different mass are available. Such measurements have been done earlier for individual CIV components, using the CIV and SiIV profiles of strong CIV systems (Rauch et al 1996). A typical value for the turbulent line of sight RMS velocity contribution to the width of individual CIV profiles was found to be

$$v_{\text{loS}} = \sqrt{\frac{1}{2}} b_{\text{turb}} = \sqrt{\frac{1}{2} \left( b^2 - \frac{2kT}{m} \right)} \simeq 4.5 \text{ km s}^{-1}, \quad (10)$$

where  $b_{\text{turb}}$  is the turbulent Doppler parameter of the CIV line,  $b$  is the total Doppler parameter, and  $T$  is the temperature.

The turbulence *along* the line of sight may be compared with the turbulence *across* the lines of sight. For this comparison we need to make an assumption about

---

<sup>4</sup>The value of  $\epsilon$  and the actual amount of turbulence in CIV systems could be somewhat smaller than that derived above. Our ability to measure very small values of  $B(r)$  ( $< \text{a few km}^2\text{s}^{-2}$ ) is limited by the measurement errors of  $v_A$  and  $v_B$ . As mentioned above, there may be additional sources of velocity shear, e.g., gravitationally induced bulk motions. In addition, it is not clear how to distinguish velocity shear from density differences across the lines of sight. (Column) density fluctuations as caused, e.g., by clumpiness in an otherwise laminar flow could mimic turbulent motions.

the typical size of individual CIV clouds. If a fiducial value of 300 pc is adopted once more, Fig.15 gives the RMS velocity difference across the sky,

$$\sqrt{v_r^2} \simeq \sqrt{B(300\text{pc})} \approx 4.7 \text{ km s}^{-1} \quad (11)$$

(as read from the value of  $B(r)$  for single components, in the central bin). The good agreement between the turbulent measurements across and along the line of sight indicates that the typical size adopted has the right order of magnitude.

A comparison of the turbulent Doppler parameters of CIV systems with other astrophysical environments is shown in Fig.16. The diagram gives the relation between the turbulent Doppler parameter and cloud size for a compilation of measurements from molecular clouds (dashed line) and HII regions (dotted line) by O’Dell (1991). The figure shows the power law fits to the data given by O’Dell. The arrows represent the upper limits to the CIV Doppler parameters from Rauch et al (1996) and the lower limits to the cloud sizes from the present work. Clearly, the turbulent motion along the line of sight observed for the C IV absorbers is smaller for a given cloud size than the values found in HII- or star-forming regions.

There is other evidence suggesting that the small scale structure of the typical high redshift CIV absorbing gas differs from that of high ionization gas detected locally (i.e., in the Milky Way or the Magellanic Clouds). Multiple lines of sight to the Magellanic Clouds show the gas to be fragmented on much smaller scales (e.g, Songaila et al 1986) than found here; the CIV column density appears to be fluctuating by 50% on parsec scales (Wakker et al 1998). However, even without invoking evolution in the physical state of the CIV gas these differences between high and low redshift absorbers are perhaps not too surprising. We are selecting high  $z$  absorption systems randomly by absorption cross-section so the observations are weighted towards large impact parameters from the nearest galaxy.

### 3.3. Origin of the velocity structure

Could the observed velocity scatter be residual turbulence from an earlier phase of metal ejection ? In a steady state, the energy transfer rate  $\epsilon$  is not only the rate at which energy is fed to the gas, but it also equals the dissipation rate. We may estimate the approximate time scale for dissipation, i.e., the time it takes to transform

the mean kinetic energy  $1/2 \langle v^2 \rangle$  in the gas, at a rate  $\epsilon$  into heat,

$$\tau_{diss} \sim \frac{1 \langle v^2 \rangle}{2 \epsilon} \sim 9 \times 10^7 \text{years}. \quad (12)$$

Apparently, energy is being dissipated at a rate fast enough to destroy turbulence on a time scale of 100 million years. Thus the turbulence we observe near the mean redshift  $\langle z \rangle \sim 2.7$  of our sample must have been produced closer to the epoch of observation and at redshifts lower than assumed for the Population III process described by, e.g., Gnedin & Ostriker (1997). The same authors find that the metallicity of the IGM produced by a true Pop III star-formation phase (at  $z \sim 7 - 10$ ) is on the level of  $10^{-4}Z_{\odot}$ , two orders of magnitude less than observed at redshifts  $< 4$ . Our inferences are *consistent* with most of the metals in the CIV clouds, together with their turbulent motions, being produced close to the epoch of observation, at least for  $z < 5$ ; this does not preclude the possibility that the process started already at much higher redshifts.

An energy input close to the epoch of observation is also indicated by what one might call "cosmic seismometry": assume that there are recurrent events (SN explosions, stellar winds, mergers) stirring up the CIV enriched gas, with a typical interval  $\tau_s$  between two such occurrences. Any density gradients in the CIV gas caused by such processes would be damped out by pressure waves propagating with the speed of sound over a spatial distance  $r$  given by the product of the sound crossing time  $\tau_s$  and the sound speed,  $c_s$ . Conversely, if there is little structure over a distance  $r$ , then there cannot have been a hydrodynamic disturbance during the past

$$\tau_s \sim \frac{r}{c_s} \approx 1.4 \times 10^7 \left( \frac{r}{300\text{pc}} \right) \left( \frac{c_s}{20\text{kms}^{-1}} \right)^{-1} \text{years}. \quad (13)$$

This number agrees to within a factor of a few with the dissipation time scale derived above. We may take these estimates as a measure of the frequency of disturbing events (probably bursts of star-formation) in the vicinity of the absorbing gas. They indicate that the regions giving rise to CIV absorption, while not *currently* experiencing gasdynamical disturbances, may have done so in the recent past and may continue to do so on a time-scale on the order of  $10^7 - 10^8$  years.

Which physical processes could conceivably stir up the gas ? We can compare the above crude estimates with other galactic time scales relevant for large scale gasdynamical effects:

If the turbulent energy in the CIV gas has been injected by galactic outflows one should expect the duty cycle of star formation to provide the relevant timescales.

At  $10^7$  years the lifetimes of star-forming molecular clouds (Shu, Adams & Lizano 1987), and the dynamical ages for hot superbubbles in local dwarf galaxies (Martin 1998), show the same order of magnitude as the above measurement. Fluctuations in the star formation rate in nearby spirals (Tomita, Tomita & Saito 1996; Hirashita & Kamaya 2000) and in galactic nuclei (Krügel & Tutukov 1992) may reccur every  $10^7 - 10^8$  years, while Glazebrook et al (1999) and Rocha-Pinto et al (2000) find typical intervals of  $2 \times 10^8$  years between maxima in the star-formation rate for their sample of  $z \sim 1$  field galaxies, and the Milky Way, respectively.

As an alternative to stellar feedback, it is conceivable that mergers or collisions (which Gnedin (1998) requires to account for the observed metal enrichment) are also capable of stirring the gas to the degree observed here. The merger rate is highly dependent on the environment and the redshift. CIV absorbers are thought to reside mostly in or between low mass halos moving within the filamentary large scale structure (Rauch, Haehnelt & Steinmetz 1997). Within the filaments the average interaction rate may be much higher than in the field. Menci & Valdarnini (1994) predict the mean intervals between merger events in the more massive filaments to range between  $5 \times 10^7$  and  $2 \times 10^8$  years, depending on the mass of the filamentary structures, which again is consistent with our estimates.

#### 4. Conclusions

Based on the observations of CIV absorption systems in closely spaced lines of sight to background QSOs we have obtained several new results on the properties of gas causing the intervening high ionization absorption systems:

(1) the CIV systems from the combined sample of three lensed QSOs, UM673, HE1104-1805, and Q1422+231 show that absorption systems with redshifts between those of the lensing galaxy and the QSO are increasingly different with redshift. This result shows that the objects are truly lensed QSOs and not QSO pairs.

(2) We found that the density and velocity structure of CIV absorbing gas at high redshift is typically featureless on scales smaller than a few hundred parsecs. Significant differences between the absorption patterns begin to emerge for separations on the order of kiloparsecs.

(3) The overall sizes of the CIV systems cannot be probed very well with lensed

QSOs because the beam separations available tend to be too small, but simple estimates based on the observations presented here imply that CIV systems extend at least over distances on the order 10 kpc along the line of sight. This is consistent with other estimates of the sizes from galaxy-absorber correlations (Bergeron & Boissé 1991, Steidel 1993).

(4) A crude measurement of the turbulence in the gas as a function of projected separation on the plane of the sky indicates a small rate of energy input,  $\epsilon \sim 10^{-3} \text{ cm}^2\text{s}^{-3}$ . Turbulent motions along the line of sight as derived from the width of absorption line profiles also point to a rather quiescent gas, unlike any known galactic environments. The CIV absorbing clouds are too 'smooth' for their size to be, e.g., HII regions. Both the amplitude of the turbulence, and the coherence length of the clouds are consistent with the clouds being affected (produced, stirred, or destroyed) by star-formation or merger-triggered gas-dynamics on a timescale of  $10^7 - 10^8$  years.

Realistic numerical studies of the gasdynamics of these processes on sub-kpc scales, and observations of close QSO images with high resolution spectrographs and adaptive optics to resolve images with sub-arcsecond separations would both be desirable for the future.

We are grateful to Bob Carswell, John Webb, Andrew Cooke and Mike Irwin for sharing the VPFIT profile fitting software, and to Bob Carswell for ample advice and help in using it, and to the Keck Observatory personnel for their help with the observations. MR thanks Matthias Steinmetz for discussions and is grateful to the ESO Office of Science for travel support, and to the Institute for Theoretical Physics at the University of Santa Barbara and the organizers of the workshop on "Galaxy Formation and Evolution" for hospitality during February and March 2000 (where the research was supported in part by the National Science Foundation under grant No. PHY99-07949). The work of WLWS was supported by NSF grant AST-9900733.

## REFERENCES

- Avni, Y., Solta, A., Tananbaum, H., Zamorani, G., 1980, ApJ238, 800  
Barlow, T.A., Sargent, W.L.W., 1997, AJ, 113, 136  
Bechtold, J., Crotts, A.P.S., Duncan, R.C., Fang, Y., 1994, ApJ, 437, 83

- Bechtold, J., & Yee, H. K. C. 1995, *AJ*, 110, 1984
- Bergeron, J., Boisse, P., 1991, *A&A*, 243, 344
- Carswell, R.F., Webb, J.K., Cooke, A.J., Irwin, M.J., 1992, Institute of Astronomy, Cambridge, <http://www.ast.cam.ac.uk/rfc/vpfit.html>
- Carswell, R.F., Webb, J.K., Lanzetta, K.M., Parnell, H.C., Webb, J.K., 1991, *ApJ*, 371, 36
- Chandrasekhar, S., 1948, *ApJ*, 110, 329
- Cowie, L.L., Songaila, A., Kim, T.-S., Hu, E.M., 1995, *AJ*, 109, 1522
- Cowie, L.L., Songaila, A., 1998, *Nature*, 394, 44
- Crotts, A.P.S., Bechtold, J., Fang, Y., Duncan, R.C., 1994, *ApJ*, 437, L79
- Dinshaw, N., Impey, C.D., Foltz, C.B., Weymann, R.J., Chaffee, F.H., 1994, *ApJ*, 437, 87
- Dinshaw, N., Foltz C.B., Impey C.D., Weymann R..J, Morris S.L., 1995, *Nature*, 373, 223
- Fang, Y., Duncan, R.C., Crotts, A.P.S., Bechtold, J., 1996, *ApJ*, 462, 77
- Fransson C., Epstein R., 1982, *MNRAS*, 198, 1127
- Ellison, S.L., Songaila, A., Schaye, J., Pettini, M., 2000, *AJ*, 120, 1175
- Fall, S.M., Rees, M.J., 1985, *ApJ*, 298, 18
- Foltz, C.B., Weymann, R.J., Röser, H.J., Chaffee, F.H., 1984, *ApJ*, 281, 1
- Glazebrook K., Blake C., Economou F., Lilly S., Colless M., 1999, *MNRAS*, 306, 843
- Gnedin, N.Y., Ostriker J.P., 1997, *ApJ*, 486, 581
- Gnedin, N.Y., 1998, *MNRAS*, 294, 407
- Hirashita H., Kamaya H., 2000, *ApJ*, 120, 728
- Kang, H., Shapiro, P.R., Fall, S.M., Rees, M.J., 1990, *ApJ*, 363, 488
- Kaplan S.A., Pikelner S.B., "The Interstellar Medium", Harvard University Press; Cambridge 1970
- Kundic, T., Hogg, D.W., Blandford, R.D., Cohen, J.G., Lubin, L.M., Larkin, J.E., 1997, *AJ*, 114, 2276
- Lidman, C., Courbin, F., Kneib, J.P., Golse, G., Castander, E., Soucail, G., 2001, *A&A*(in press). See also astro-ph/0010403.

- Lopez, S., Reimers, D., Rauch, M., Sargent, W.L.W., Smette, A., 1999, ApJ, 513, 598
- Martin C.L., 1998, ApJ, 506, 222
- Menci N., Valdarnini R., 1994, ApJ, 436, 559
- Michalitsianos, A.G., Dolan J.F., Kazanas, D., Bruhweiler, F.C., Boyd, P.T., Hill, R.J., Nelson, M.J., Percival, J.W., van Citters, G.W., 1997, ApJ, 487, L117
- Monier, E.M., Turnshek, D.A., Lupie, O.L., 1998, ApJ, 496, 177
- Morris, S.L., van den Bergh, S., 1994, ApJ, 427, 696
- McGill C., 1990, MNRAS, 242, 544
- Mo, H.J., Miralda-Escudé, J., 1996, ApJ, 469, 589
- Münch, G., 1958 in: *Cosmical Gas Dynamics*, Eds. J. M. Burgers, R.N. Thomas. International Astronomical Union. Symposium no. 8, p. 1035
- O'Dell, C.R., 1991, in: E. Falgarone et al (eds.) *Fragmentation of Molecular Clouds and Star Formation* 476-479, IAU 1991.
- Patnaik, A.R., Browne, I.W.A., Walsh, D., Chaffee, F.H., Foltz, C.B., 1992, MNRAS, 259, 1
- Peng, W., Weisheit, J.C., 1991, ApJ, 373, 471
- Petitjean, P., Bergeron, J., 1994, A&A, 283, 759
- Petitjean, P., Aracil, B., Srianand, R., Ibata, R. 2000, A&A, 359, 457
- Petry, C.E., Impey, C.D., Foltz, C.B., 1998, ApJ, 494, 60
- Press W.H., Flannery B.P., Teukolsky S.A., Vetterling W.T., *Numerical Recipes*, Cambridge University Press, Cambridge: 1986.
- Rauch, M., Haehnelt, M.G., Steinmetz, M., 1997, ApJ, 481, 601
- Rauch, M., Sargent, W.L.W., Womble, D.S., Barlow, T.A., 1996, ApJ, 467, L5
- Rauch, M., Sargent, W.L.W., Barlow, T.A., 1999, ApJ, 515, 500
- Rocha-Pinto H.J., Scalo J., Maciel W.J., Flynn C., 2000, ApJ, 531, L115
- Sargent, W.L.W, Young, P.J., Boksenberg, A., Carswell, R.F., Whelan, J.A.J., 1979, ApJ, 230, 49
- Sargent, W.L.W., Young, P.J., Schneider, D.P., 1982, ApJ, 256, 374
- Sargent, W.L.W, Steidel, C.C., Boksenberg, A., 1988, ApJS, 68, 539

- Scalo, J.M., 1984, ApJ, 277, 556
- Schaye, J., Rauch, M., Sargent, W.L.W., Kim, T.-S., 2000, ApJ541, L1
- Shaver, P.A., Robertson, J.G., 1983, ApJ, 268,57
- Shu F.H., Adams F.C., Lizano S., 1987, ARA&A, 25, 23
- Smette, A., Surdej, J., Shaver, P.A., Foltz, C.B., Chaffee, F.H., Weymann, R.J., Williams, R.E., Magain, P., 1992, ApJ, 389, 39
- Smette, A., Robertson, J.G., Shaver, P.A., Reimers, D., Wisotzki, L., Koehler, T., 1995, A&A, 113, 199
- Songaila, A., Blades, J.C., Hu, E.M., Cowie, L.L., 1986, ApJ, 303, 198
- Steidel, C.C., 1990, ApJS, 74, 37
- Steidel, C.C., 1993, in: *Galaxy Evolution: The Milky Way Perspective*. ASP Conference Series 49. ed. Majewski, S. Astronomical Society of the Pacific,
- Surdej, J., Magain, P., Swings, J.-P., Borgeest, U., Courvoisier, T.J.-L., Kayser, R., Kellermann, K.I., Kuhr, H., Refsdal, S.,1988, A&A, 198, 49
- Tomita A., Tomita Y., Saito M., 1996, PASJ, 48, 285
- Tytler, D., Fan, X.-M., Burles, S., Cottrell, L., Davis, C. et al., 1995, In *QSO Absorption Lines*. ed. Meylan G. Berlin: Springer
- Vogt, S.S., et al., 1994, *S.P.I.E.* 2198, 362
- von Hoerner S., Z.Astrophys. 30, 17
- Wakker, B., Howk, J.C., Chu, Y.-H., Bomans, D., Points, S.D., 1998, ApJ, 499, L87
- Wang, B., 1993, ApJ, 415, 174
- Wang, B., 1995, ApJ, 444, L17
- Wisotzki, L., Köhler, T., Kayser, R., Reimers, D., 1993, A&A, 278, 14
- Wisotzki, L., Wucknitz, O., Lopez, S., Sorensen, A.N., 1998, A&A, 339, L37
- Womble, D.S., Sargent, W.L.W., Lyons, R.S., 1996. in: *Cold Gas at High Redshift* p. 137. (eds.) Bremer MN et al. Kluwer
- Young, P.J., Sargent, W.L.W., Boksenberg, A., Oke, J.B. 1981, ApJ, 249, 415

Zuo, L. Beaver, E.A., Burbidge, E.M., Cohen, R.D., Junkkarinen, V.T. Lyons, R.W.,  
1997, ApJ, 477, 568

---

This preprint was prepared with the AAS L<sup>A</sup>T<sub>E</sub>X macros v5.0.

Table 1. Comparison of CIV systems towards Q1422+231

#	$N_A$	$N_B$	$\Delta \log N$	$\overline{v_A} - \overline{v_B}$	$\Delta v_A$	$\Delta v_B$	
$z = \mathbf{2.665}$ $r = 0.41 \text{ h}_{50}^{-1} \text{ kpc}$							
1	$1.06E+13$	$6.67E+12$	0.37	16.20	150.49	223.19	1 0 0
2	$3.47E+12$	$4.79E+12$	-0.28	-8.72	-	-	0 0 3
$z = \mathbf{2.68}$ $r = 0.395 \text{ h}_{50}^{-1} \text{ kpc}$							
1	$1.40E+13$	$1.81E+13$	-0.22	-9.86	106.87	85.06	1 0 0
2	$8.32E+13$	$1.25E+14$	-0.34	-0.91	-	12.36	0 0 3
$z = \mathbf{2.697}$ $r = 0.386 \text{ h}_{50}^{-1} \text{ kpc}$							
1	$4.04E+13$	$4.44E+13$	-0.09	-11.19	203.56	212.28	1 0 0
2	$1.12E+13$	$9.08E+12$	0.19	-0.28	10.18	11.63	0 0 3
3	$2.17E+13$	$2.45E+13$	-0.11	-1.13	17.45	38.53	0 2 0
$z = \mathbf{2.72}$ $r = 0.372 \text{ h}_{50}^{-1} \text{ kpc}$							
1	$6.69E+12$	$8.10E+12$	-0.17	-5.27	29.08	24.72	1 0 0
$z = \mathbf{2.75}$ $r = 0.356 \text{ h}_{50}^{-1} \text{ kpc}$							
1	$5.46E+13$	$4.57E+13$	0.16	-7.50	81.42	104.69	1 0 0
2	$4.11E+13$	$2.88E+13$	0.30	1.55	24.72	20.36	0 2 0
3	$6.76E+12$	$1.12E+13$	-0.40	-12.16	-	21.81	0 0 3
$z = \mathbf{2.77}$ $r = 0.342 \text{ h}_{50}^{-1} \text{ kpc}$							
1	$1.74E+12$	$1.41E+12$	0.19	-2.91	-	-	1 0 3
$z = \mathbf{2.80}$ $r = 0.329 \text{ h}_{50}^{-1} \text{ kpc}$							
1	$5.37E+12$	$7.76E+12$	-0.31	21.71	-	60.34	1 0 0
$z = \mathbf{2.90}$ $r = 0.277 \text{ h}_{50}^{-1} \text{ kpc}$							
1	$1.32E+13$	$1.41E+13$	-0.07	-0.65	36.35	69.79	1 0 0
$z = \mathbf{2.95}$ $r = 0.252 \text{ h}_{50}^{-1} \text{ kpc}$							
1	$5.94E+12$	$5.60E+12$	0.06	-2.68	172.30	165.76	1 0 0
2	$2.63E+12$	$2.51E+12$	0.05	-7.27	-	-	0 2 3
3	$3.31E+12$	$3.09E+12$	0.07	-0.73	-	-	0 2 3
$z = \mathbf{2.97}$ $r = 0.240 \text{ h}_{50}^{-1} \text{ kpc}$							
1	$1.14E+13$	$1.35E+13$	-0.15	12.67	363.50	367.14	1 0 0
2	$3.02E+12$	$4.14E+12$	-0.27	-3.20	-	14.54	0 2 3
3	$8.40E+12$	$9.32E+12$	-0.10	-2.27	37.08	31.99	0 2 0
4	$6.31E+12$	$7.08E+12$	-0.11	-0.73	-	-	0 0 3

Table 1—Continued

#	$N_A$	$N_B$	$\Delta \log N$	$\bar{v}_A - \bar{v}_B$	$\Delta v_A$	$\Delta v_B$	
$z = \mathbf{3.00}$ $r = 0.227 h_{50}^{-1} \text{ kpc}$							
1	$5.01E+12$	$5.89E+12$	-0.15	-2.91	—	—	1 0 3
$z = \mathbf{3.06}$ $r = 0.199 h_{50}^{-1} \text{ kpc}$							
1	$1.22E+13$	$1.82E+13$	-0.33	-4.80	585.23	585.23	1 0 0
2	$9.59E+12$	$1.47E+13$	-0.35	-15.26	91.60	82.15	0 2 0
3	$2.57E+12$	$3.55E+12$	-0.28	-8.00	—	—	0 2 3
4	$6.78E+12$	$7.27E+12$	-0.07	-2.30	28.35	19.63	0 0 3
5	$2.82E+12$	$7.41E+12$	-0.62	1.45	—	—	0 0 3
$z = \mathbf{3.09}$ $r = 0.187 h_{50}^{-1} \text{ kpc}$							
1	$4.33E+13$	$4.30E+13$	0.01	-4.35	87.24	87.97	1 0 0
2	$9.55E+12$	$1.05E+13$	-0.09	0.73	—	—	0 0 3
$z = \mathbf{3.13}$ $r = 0.169 h_{50}^{-1} \text{ kpc}$							
1	$3.38E+13$	$2.95E+13$	0.13	-9.00	402.76	423.84	1 0 0
2	$2.36E+13$	$2.09E+13$	0.12	-14.43	148.31	146.85	0 2 0
3	$1.02E+13$	$8.67E+12$	0.15	-2.83	103.96	87.97	0 2 0
4	$6.92E+12$	$7.29E+12$	-0.05	-1.26	—	17.45	0 0 3
5	$4.68E+12$	$5.25E+12$	-0.11	-2.18	—	—	0 0 3
$z = \mathbf{3.27}$ $r = 0.117 h_{50}^{-1} \text{ kpc}$							
1	$4.68E+12$	$4.47E+12$	0.05	—	—	—	1 0 3
$z = \mathbf{3.41}$ $r = 0.066 h_{50}^{-1} \text{ kpc}$							
1	$8.13E+12$	$8.48E+12$	-0.04	-6.35	—	5.09	1 0 0
$z = \mathbf{3.53}$ $r = 0.027 h_{50}^{-1} \text{ kpc}$							
1	$2.30E+14$	$2.38E+14$	-0.03	2.81	426.02	434.02	1 0 0
2	$4.53E+13$	$4.55E+13$	0.00	-2.18	13.81	11.63	0 0 3
3	$2.41E+13$	$2.73E+13$	-0.12	-2.63	15.27	30.53	0 0 3
4	$6.26E+13$	$6.88E+13$	-0.09	-1.30	9.45	8.72	0 0 3
5	$.384E+13$	$3.77E+13$	0.02	-1.78	9.45	8.00	0 0 3
$z = \mathbf{3.58}$ $r = 0.016 h_{50}^{-1} \text{ kpc}$							
1	$2.25E+13$	$2.31E+13$	-0.03	6.12	145.40	148.31	1 0 0
2	$1.55E+13$	$1.70E+13$	-0.09	-0.73	—	—	0 0 3
3	$6.98E+12$	$6.08E+12$	0.13	0.26	6.54	12.36	0 0 3

Table 1—Continued

#	$N_A$	$N_B$	$\Delta \log N$	$\bar{v}_A - \bar{v}_B$	$\Delta v_A$	$\Delta v_B$			
$z = \mathbf{3.62}$			$r = 0.001 \text{ h}_{50}^{-1} \text{ kpc}$						
1	$1.01E+14$	$9.43E+13$	0.07	-2.92	74.88	58.16	1	0	0
2	$339E+13$	$2.95E+13$	0.13	-1.13	3.63	–	0	0	3
3	$5.41E+13$	$5.94E+13$	-0.09	-1.61	0.73	18.90	0	0	3

Table 2. Comparison of CIV systems towards HE1104-1805

#	$N_A$	$N_B$	$\Delta \log N$	$\overline{v_A} - \overline{v_B}$	$\Delta v_A$	$\Delta v_B$			
<b><math>z = 1.661</math></b> $r = 4.7 h_{50}^{-1}$ kpc									
1	$2.75E+14$	$4.22E+14$	-0.35	62.66	469.64	420.21	1	0	0
2	$1.59E+14$	$3.54E+14$	-0.55	-24.29	259.54	207.20	0	0	0
3	$1.16E+14$	$6.73E+13$	0.42	-20.23	131.59	61.79	0	2	0
4	$1.21E+14$	$3.00E+14$	-0.60	-44.14	40.71	59.61	0	2	0
5	$7.76E+13$	$2.59E+13$	0.67	-10.80	-	13.81	0	2	0
6	$1.05E+14$	$5.89E+13$	0.44	-27.63	-	-	0	0	3
<b><math>z = 1.747</math></b> $r = 3.9 h_{50}^{-1}$ kpc									
1	$8.32E+12$	$4.68E+12$	0.44	-1.45	-	-	1	0	3
<b><math>z = 1.859</math></b> $r = 2.9 h_{50}^{-1}$ kpc									
1	$4.45E+13$	$8.25E+13$	-0.46	50.37	251.54	303.16	1	0	0
2	$3.54E+13$	$7.23E+13$	-0.51	38.52	76.33	179.57	0	2	0
3	$9.12E+12$	$1.02E+13$	-0.10	6.37	-	33.44	0	2	0
4	$9.12E+12$	$9.33E+12$	-0.02	3.63	-	-	0	0	3
<b><math>z = 2.01</math></b> $r = 1.76 h_{50}^{-1}$ kpc									
1	not det.	$1.32E+13$	-1.00	-	-	83.61	1	0	0
<b><math>z = 2.05</math></b> $r = 1.48 h_{50}^{-1}$ kpc									
1	not det.	$7.10E+13$	-1.00	-	-	26.17	1	0	0
<b><math>z = 2.20</math></b> $r = 0.59 h_{50}^{-1}$ kpc									
1	$4.47E+13$	$9.13E+13$	-0.51	-16.96	175.21	210.83	1	0	0
2	$2.22E+13$	$7.19E+13$	-0.69	-7.57	29.81	8.72	0	2	0
3	$3.22E+12$	$1.58E+12$	0.51	-10.83	7.27	-	0	2	0
<b><math>z = 2.298</math></b> $r = 0.06 h_{50}^{-1}$ kpc									
1	$9.84E+13$	$1.41E+14$	-0.30	9.16	300.25	330.79	1	0	0
2	$7.43E+13$	$1.15E+14$	-0.35	-0.17	109.78	113.41	0	2	0
3	$2.41E+13$	$2.62E+13$	-0.08	-4.30	141.76	173.03	0	2	0
4	$4.37E+13$	$3.39E+13$	0.22	6.54	-	-	0	0	3
5	$2.56E+13$	$7.02E+13$	-0.64	10.79	10.18	12.36	0	0	3
6	$1.45E+12$	$6.46E+11$	0.55	-4.36	-	-	0	0	3
7	$1.50E+13$	$9.77E+12$	0.35	-0.26	5.82	-	0	0	3
8	$4.17E+12$	$1.13E+13$	-0.63	5.90	-	8.00	0	0	3

Table 2—Continued

#	$N_A$	$N_B$	$\Delta \log N$	$\overline{v}_A - \overline{v}_B$	$\Delta v_A$	$\Delta v_B$	
9	$1.74E+12$	$1.01E+13$	-0.83	-0.17	–	0.73	0 0 3
$z = \mathbf{2.314}$				$z_{abs} > z_{em}$			
1	$7.58E+12$	$7.72E+12$	-0.02	1.61	43.62	50.89	1 0 0
2	$6.46E+12$	$6.76E+12$	-0.05	1.45	–	–	0 0 3
3	$1.12E+12$	$9.55E+11$	0.15	-5.82	–	–	0 0 3

Table 3. Comparison of CIV systems towards UM 673 A and B

#	$N_A$	$N_B$	$\Delta \log N$	$\overline{v_A} - \overline{v_B}$	$\Delta v_A$	$\Delta v_B$		
<b><math>z = 1.940</math></b> $r = 1.70 h_{50}^{-1} \text{ kpc}$								
1	$5.41E+14$	$4.62E+14$	0.15	62.51	471.10	486.36	1	0 0
2	$3.41E+14$	$3.87E+14$	-0.12	-8.80	178.84	210.83	0	2 0
3	$2.07E+14$	$3.27E+14$	-0.37	-26.94	85.06	81.42	0	0 0
4	$3.47E+13$	$2.04E+13$	0.41	-7.27	–	–	0	0 3
5	$2.82E+13$	$2.57E+13$	0.09	-21.08	–	–	0	0 3
6	$1.99E+14$	$7.44E+13$	0.63	-5.93	117.77	117.77	0	2 0
7	$7.08E+12$	$9.55E+12$	-0.26	-4.36	–	–	0	0 3
8	$1.05E+14$	$4.79E+13$	0.54	-2.91	–	–	0	0 3
9	$2.19E+13$	$1.15E+13$	0.48	10.90	–	–	0	0 3
<b><math>z = 2.060</math></b> $r = 1.34 h_{50}^{-1} \text{ kpc}$								
1	$3.80E+13$	$5.26E+13$	-0.28	-68.66	605.59	615.04	1	0 0
2	$1.25E+13$	$1.12E+13$	0.10	4.74	28.35	–	0	2 0
3	$1.20E+13$	$1.12E+13$	0.07	3.63	–	–	0	0 3
4	$2.55E+13$	$4.13E+13$	-0.38	-5.82	51.62	57.43	0	2 0
5	$1.23E+13$	$2.24E+13$	-0.45	-19.63	–	–	0	0 3
6	$1.45E+12$	$3.47E+12$	-0.58	-5.82	–	–	0	0 3
<b><math>z = 2.355</math></b> $r = 0.63 h_{50}^{-1} \text{ kpc}$								
1	$3.79E+14$	$3.79E+14$	0.00	-17.32	285.71	311.88	1	0 0
2	$3.72E+14$	$3.69E+14$	0.01	-15.15	205.74	183.93	0	2 0
3	$6.17E+12$	$5.37E+12$	0.13	3.63	–	–	0	2 3
<b><math>z = 2.665</math></b> $r = 0.08 h_{50}^{-1} \text{ kpc}$								
1	$1.30E+13$	$1.32E+13$	-0.02	2.24	49.44	13.09	1	2 0
2	$1.15E+13$	$1.32E+13$	-0.13	-3.40	–	13.09	0	0 0
3	$1.15E+13$	$1.05E+13$	0.09	-0.73	–	–	0	0 3
<b><math>z = 2.71</math></b> $r = 0.02 h_{50}^{-1} \text{ kpc}$								
1	$9.25E+12$	$9.85E+12$	-0.06	0.61	8.72	15.99	1	2 0
<b><math>z = 2.736</math></b> $z_{abs} > z_{em}$								
1	$2.39E+13$	$2.06E+13$	0.13	18.72	272.62	305.34	1	0 0
2	$1.53E+13$	$1.52E+13$	0.01	0.08	16.72	18.90	0	2 0
3	$8.71E+12$	$8.32E+12$	0.05	1.45	–	–	0	0 3

Table 3—Continued

#	$N_A$	$N_B$	$\Delta \log N$	$\overline{v}_A - \overline{v}_B$	$\Delta v_A$	$\Delta v_B$		
4	$8.54E+12$	$5.40E+12$	0.37	-19.97	36.35	69.07	0	2 0
5	$4.07E+12$	$2.24E+12$	0.45	1.45	–	–	0	0 3
6	$4.47E+12$	$3.16E+12$	0.29	-31.26	–	–	0	0 3

5. figures

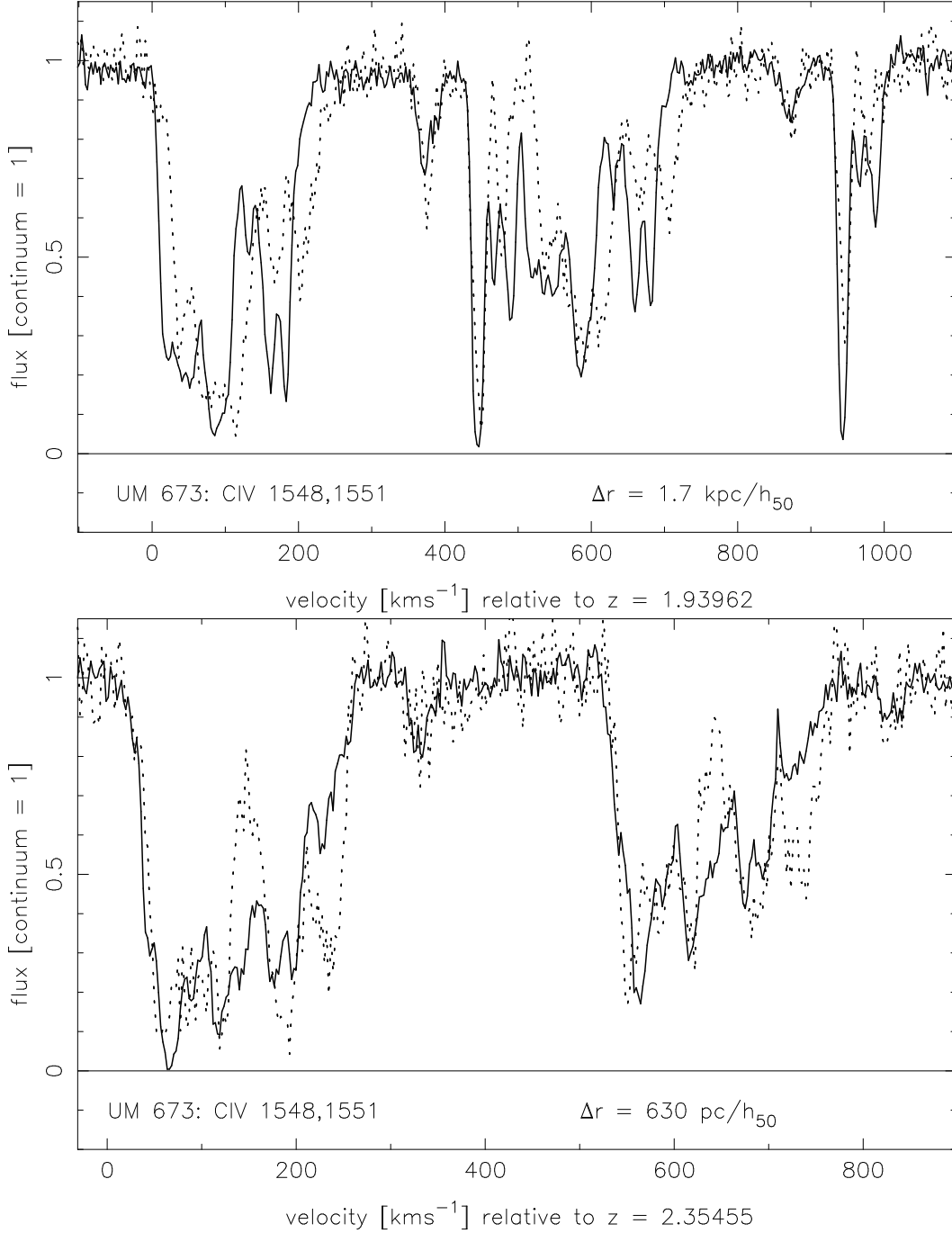


Fig. 1.— Two examples of strong CIV systems at redshifts 1.940 (top; (separation between the lines of sight:  $1.7 h_{50}^{-1}$  kpc) and 2.355 (bottom; (separation between the lines of sight:  $0.63 h_{50}^{-1}$  kpc) towards UM673. Solid line and dotted line show the spectra of the A and B image, respectively. The velocity scale applies to the rest frame of the systems. In the upper image note the different amounts of velocity shear ( $v_A - v_B$ ) for the absorption clump with  $0 < v < 250 \text{ km s}^{-1}$  and the sharp, nearly unshifted absorption line near  $450 \text{ km s}^{-1}$ . This absorption signature could be caused by a merger of two clumps of gas with different internal kinematics.

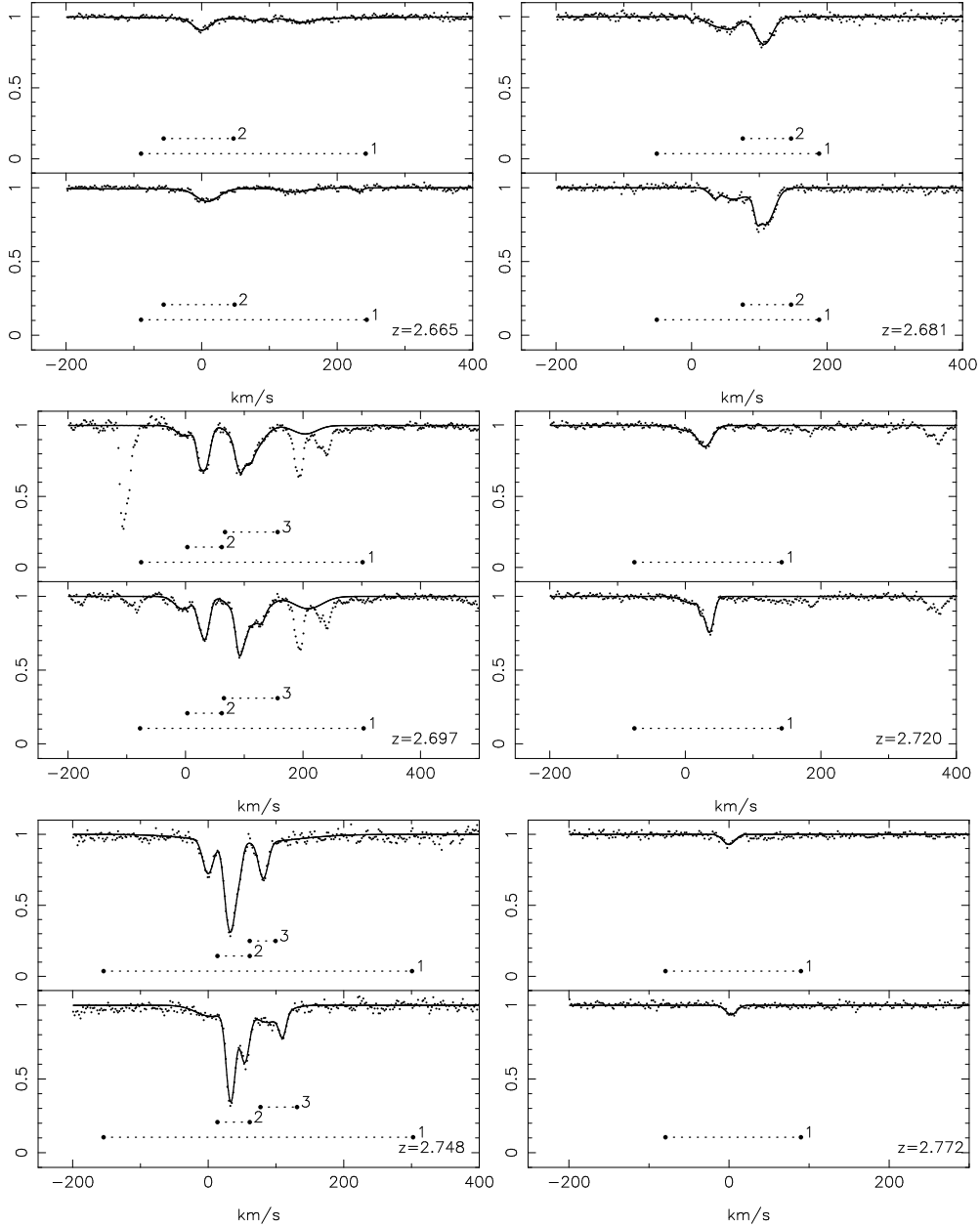


Fig. 2.— CIV systems redward of the Ly $\alpha$  emission line in the A and C lines of sight towards Q1422+231. In figures 2 – 7, the solid line in the top and bottom plots represents the Voigt profile models of the CIV  $\lambda 1548\text{\AA}$  transition in the two lines of sight. The models are plotted on top of the actual data (thin dotted line). The redshift is given in the bottom RHS corner. The horizontal dotted lines drawn underneath the spectra mark the extent of the velocity windows in which the integrated column densities and column density weighted velocities (listed in tables 1 – 3) were measured. The numbers correspond to those in the first column of these tables, for each redshift. Any absorption features not shown as fits are interlopers from other metal transitions. All blends between CIV and such lines have been fitted simultaneously but the results are shown only for CIV to avoid confusion.

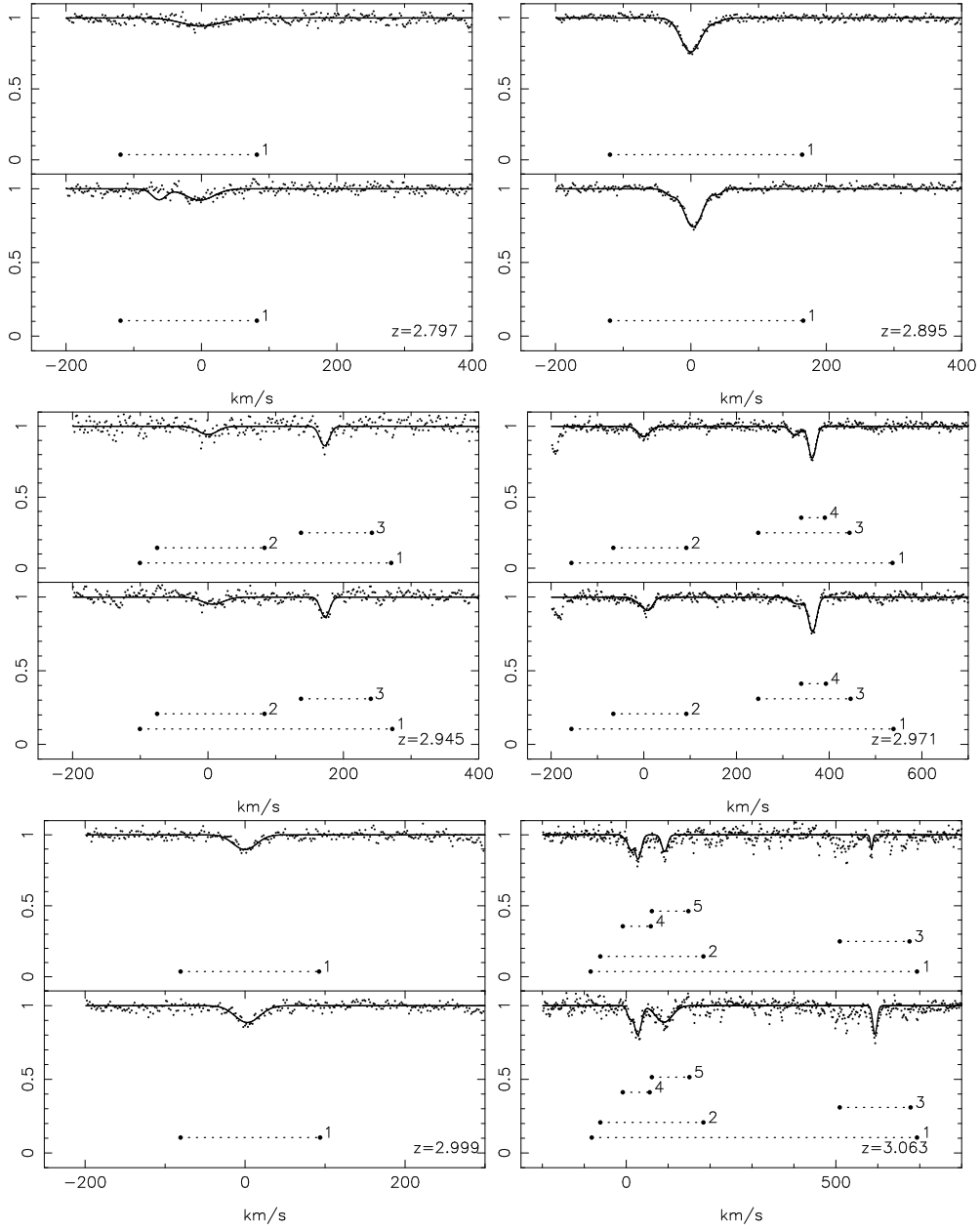


Fig. 3.— CIV systems redward of the Ly $\alpha$  emission line in the A and C lines of sight towards Q1422+231 (continued)

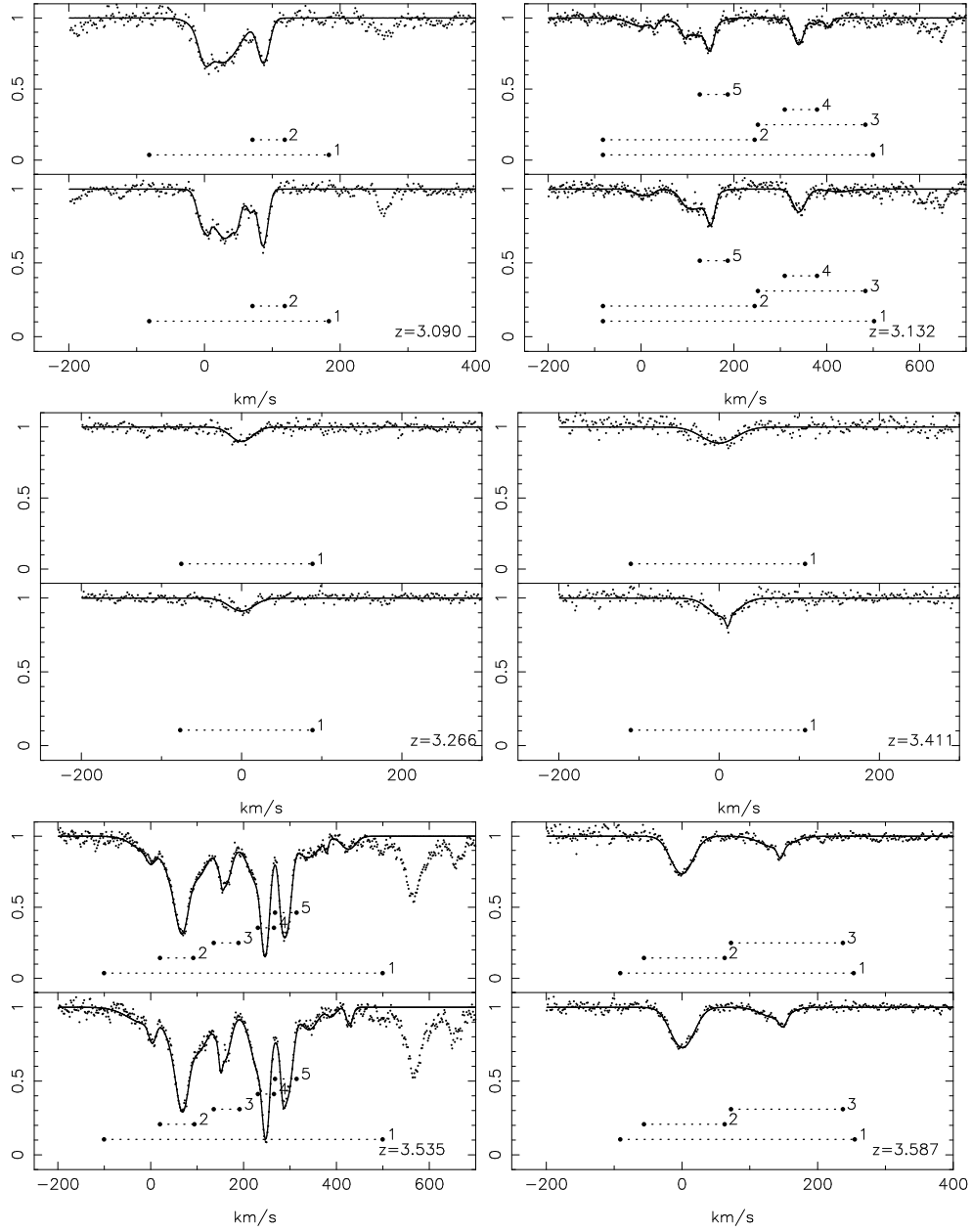


Fig. 4.— CIV systems redward of the Ly $\alpha$  emission line in the A and C lines of sight towards Q1422+231 (continued)

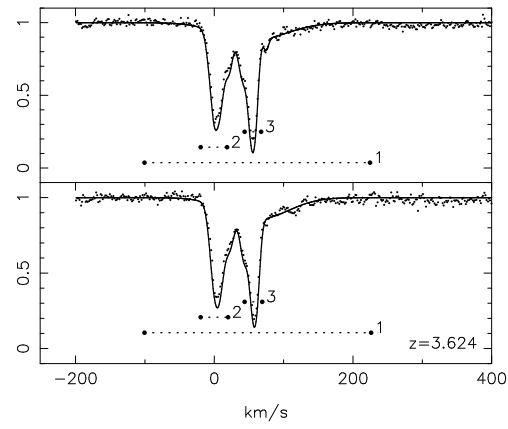


Fig. 5.— CIV systems redward of the Ly $\alpha$  emission line in the A and C lines of sight towards Q1422+231 (continued)

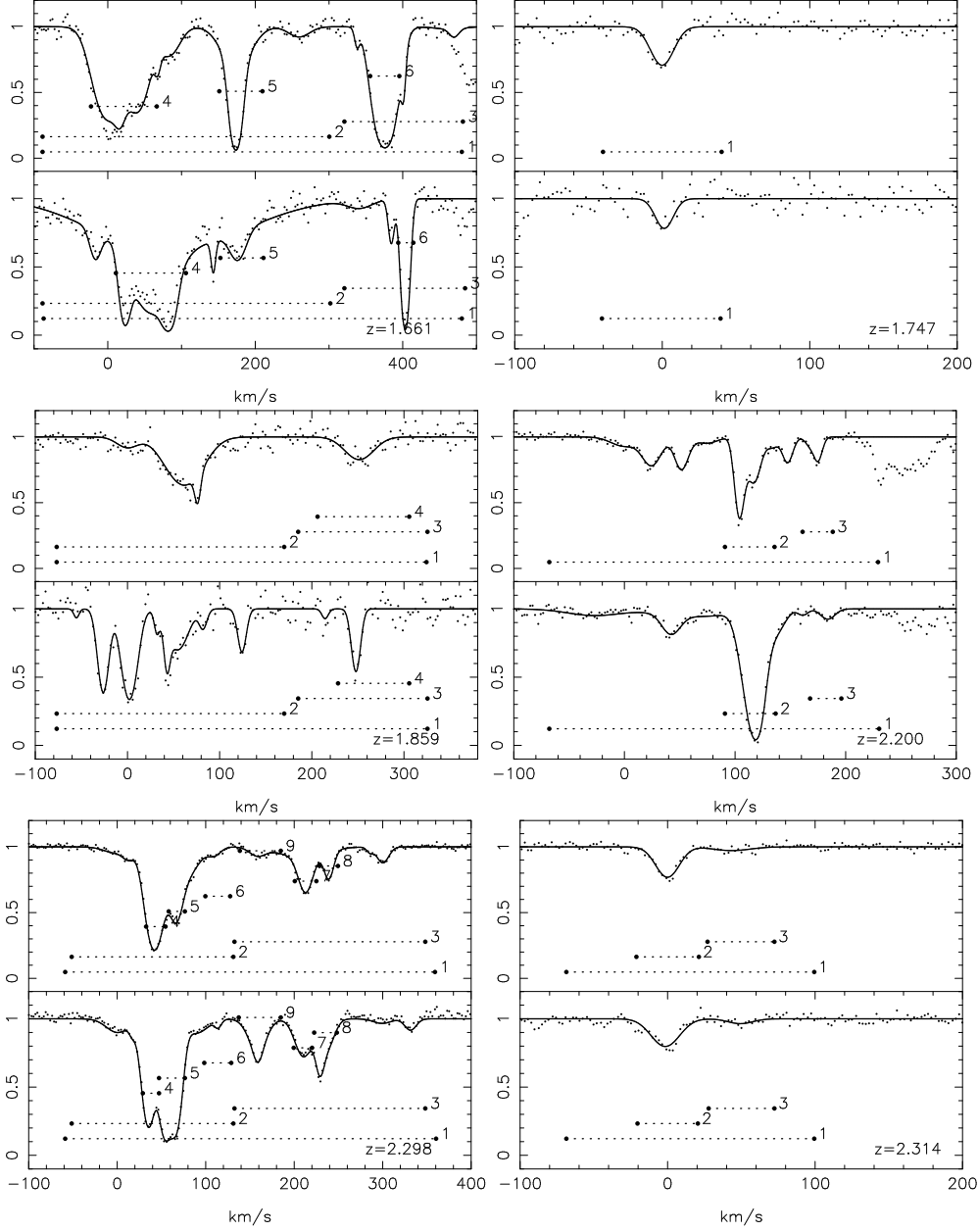


Fig. 6.— CIV systems redward of the Ly $\alpha$  emission line in the A and B lines of sight towards HE1104-1805

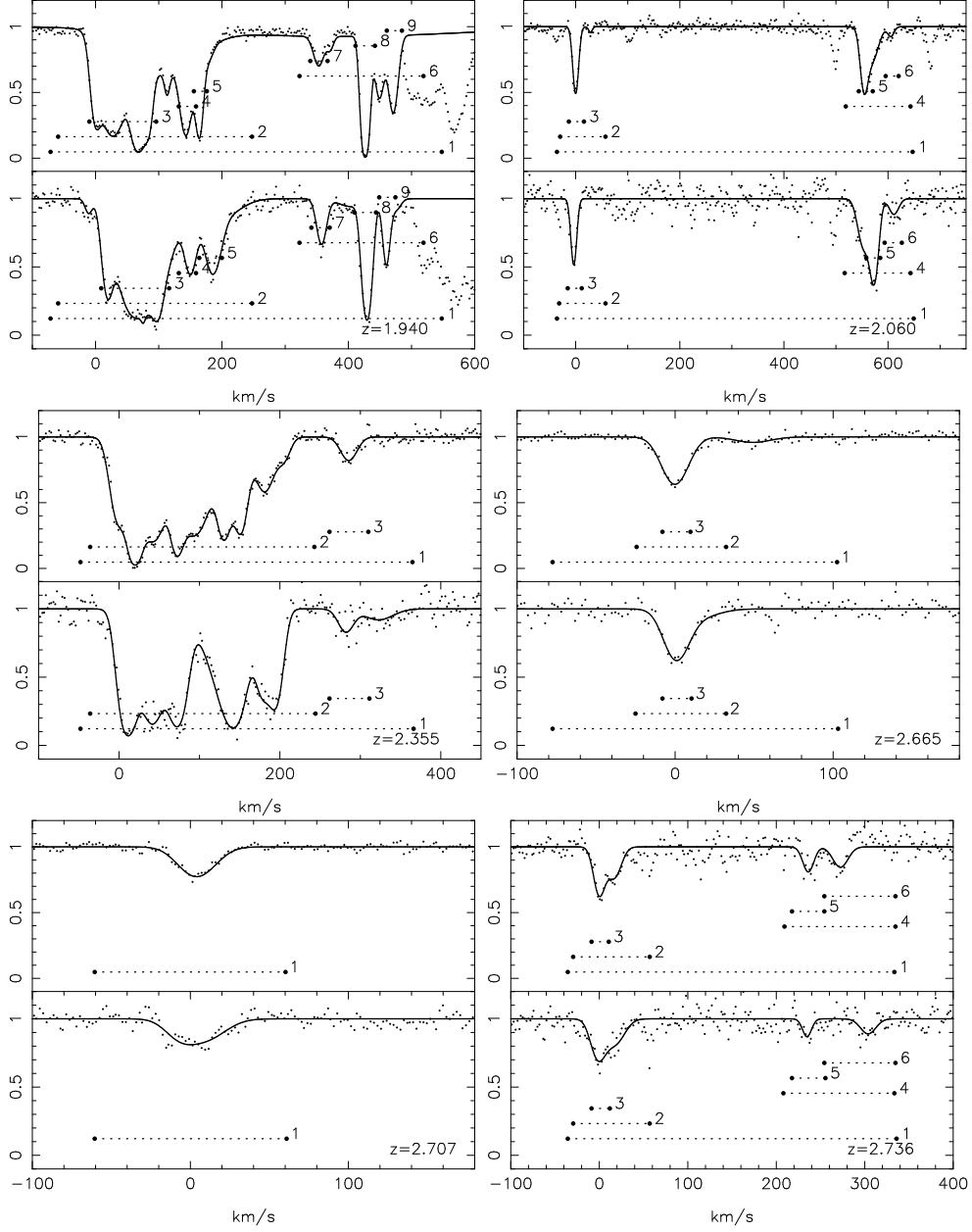


Fig. 7.— CIV systems redward of the Ly $\alpha$  emission line in the A and B lines of sight towards UM673

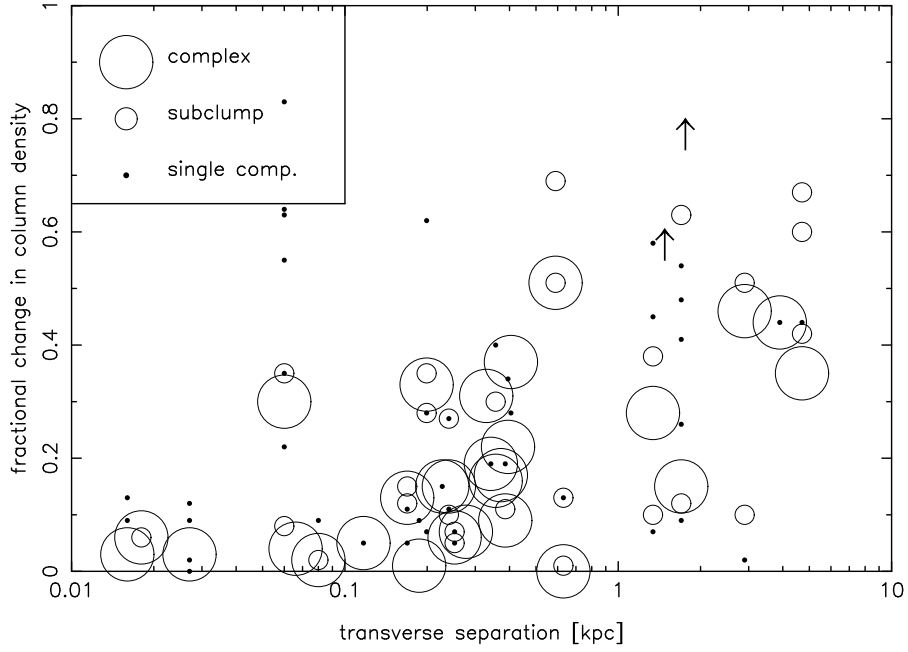


Fig. 8.— Fractional change in CIV column density as a function of transverse separation between the lines of sight. For HE1104-1805, a lens redshift of 0.73 was assumed.

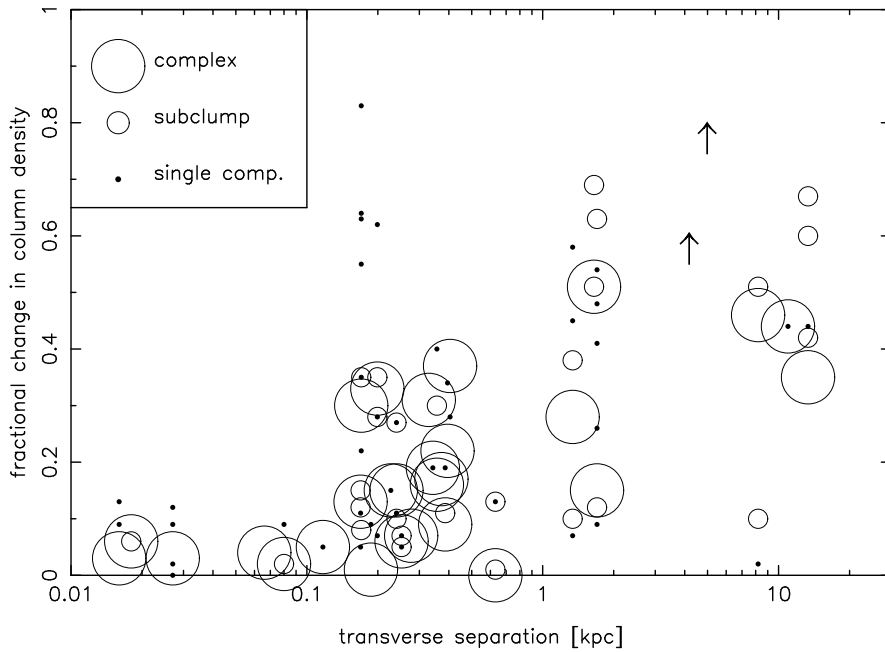


Fig. 9.— As in fig.8, but now assuming that the lens of HE1104-1805 is at  $z = 1.32$ .

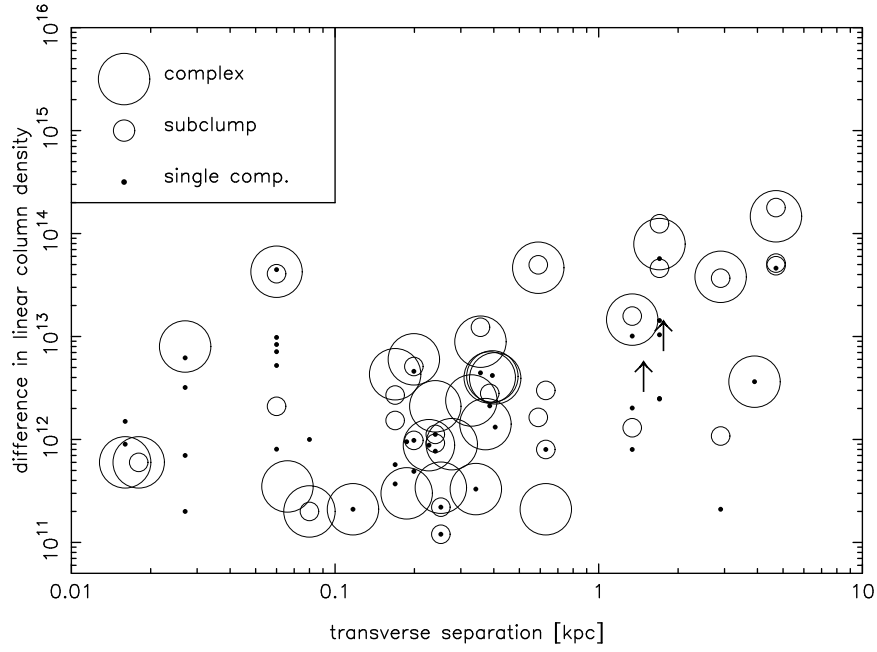


Fig. 10.— Absolute change in CIV column density as a function of transverse separation between the lines of sight, assuming  $z_{lens}(HE1104 - 1805)=0.73$ .

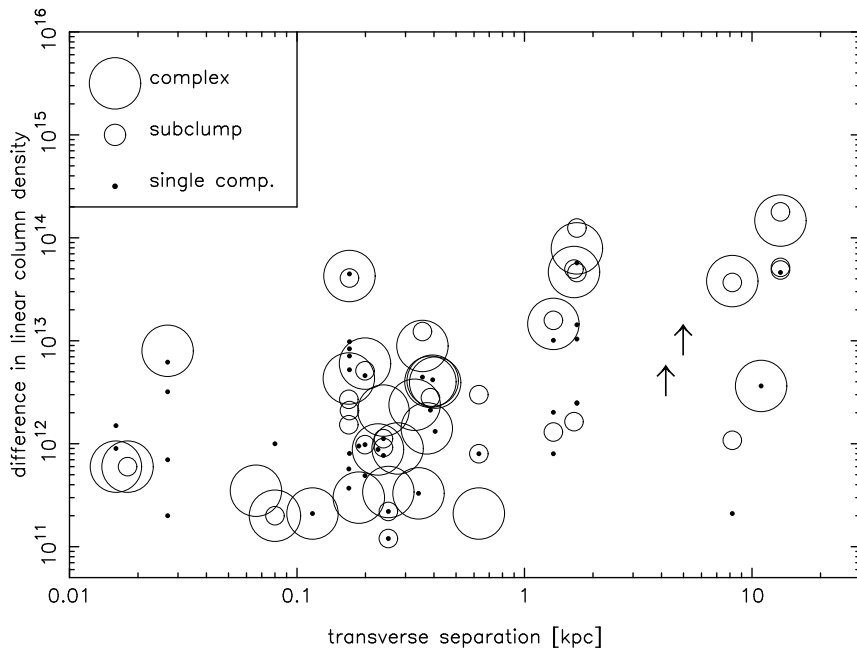


Fig. 11.— As fig. 10, but now assuming  $z_{lens}(HE1104 - 1805)=1.32$ .

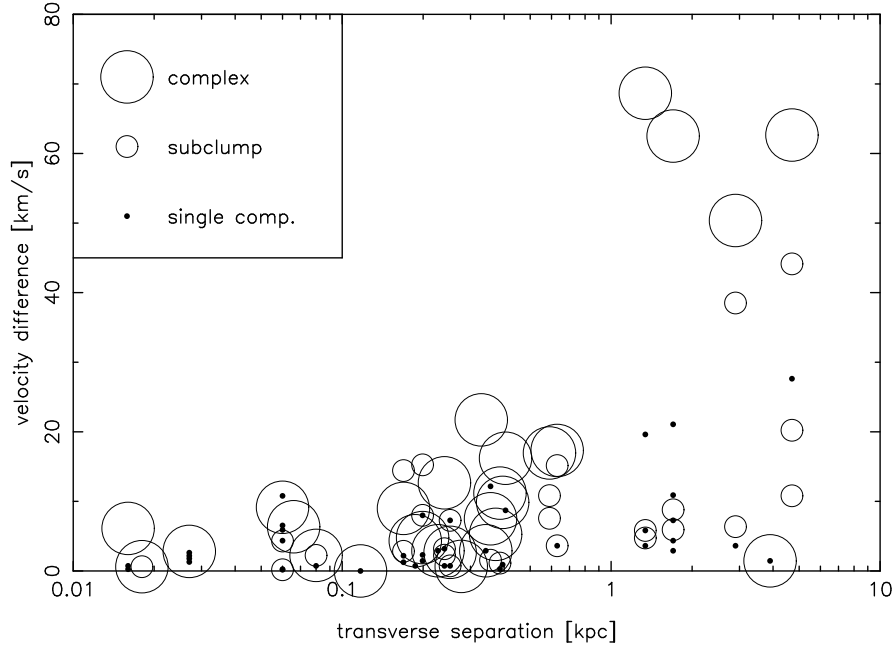


Fig. 12.— Differences between the column density weighted velocities along the line of sight, as a function of beam separation (assuming  $z_{lens}(HE1104 - 1805) = 0.73$ ).

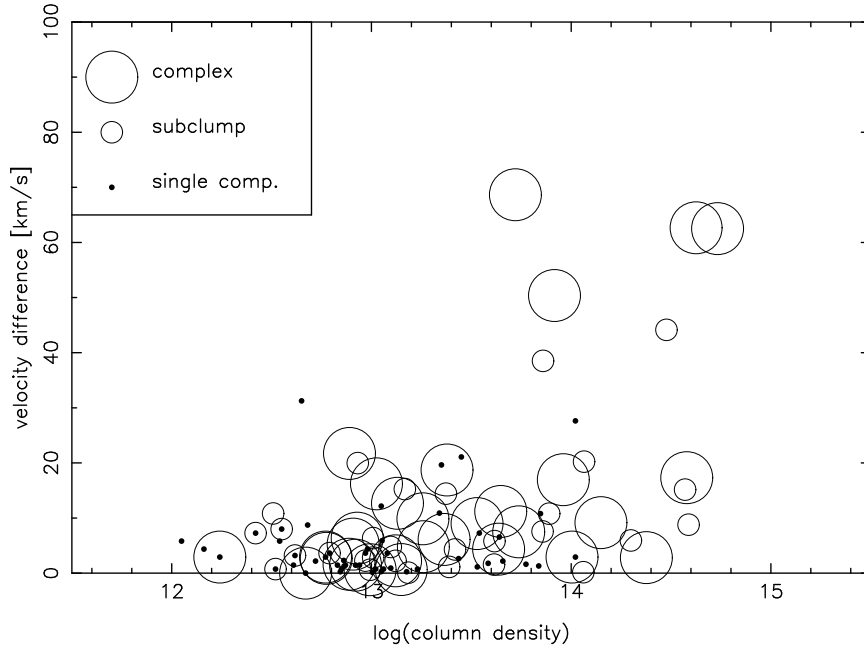


Fig. 13.— Differences between the column density weighted velocities along the line of sight, as a function of the column density (assuming  $z_{lens}(HE1104 - 1805) = 0.73$ ).

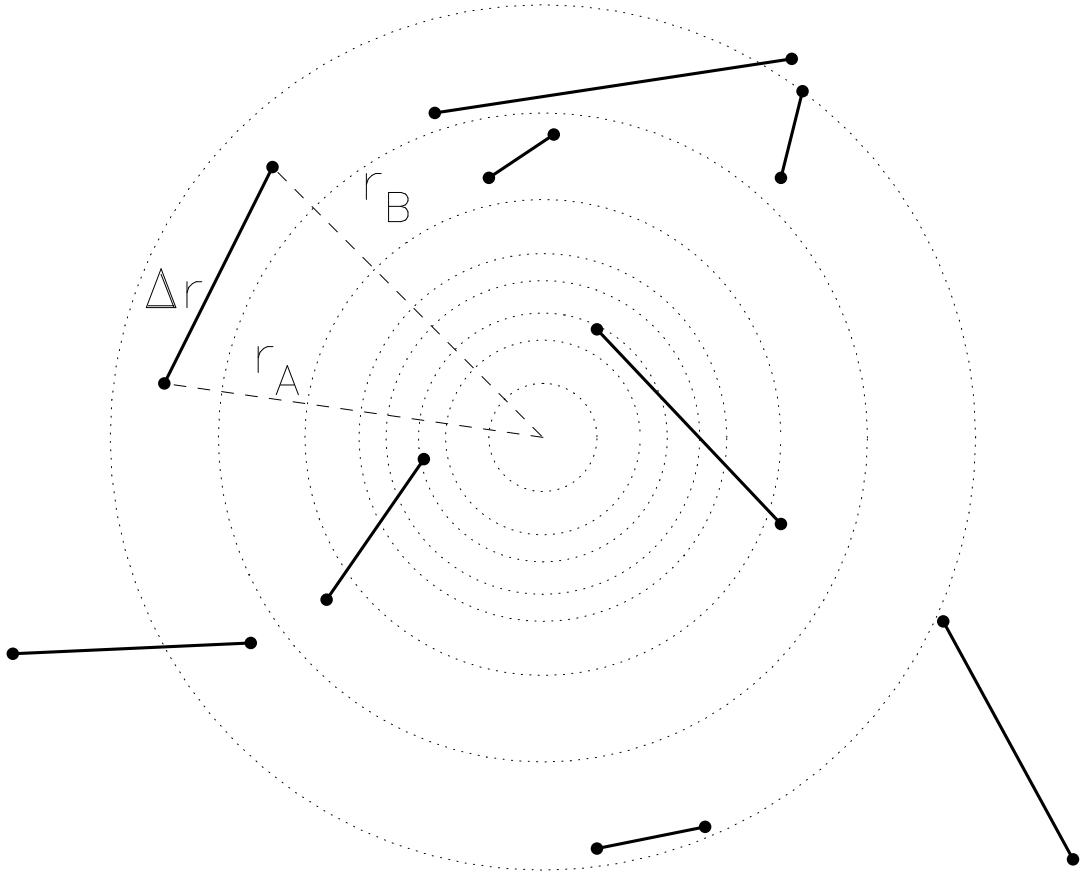


Fig. 14.— diagram illustrating the statistical reconstruction of the column density contours (dashed lines) of a simple cloud model using pairs of column density measurements from random hits by double lines of sight.

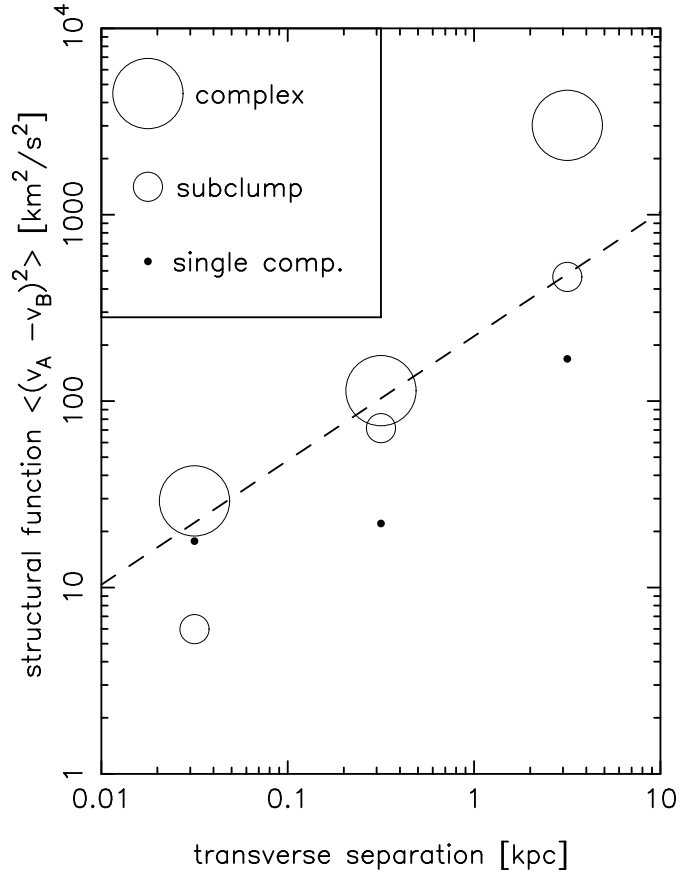


Fig. 15.— Structure function  $\langle (v_A - v_B)^2 \rangle$  as a function of beam separation. To reduce the scatter the datapoints of the previous figures have been collected in three bins. The dashed line illustrates a Kolmogorov spectrum with a vertical normalization corresponding to an energy transfer rate  $\epsilon = 10^{-3} \text{ cm}^2 \text{ s}^{-3}$ .

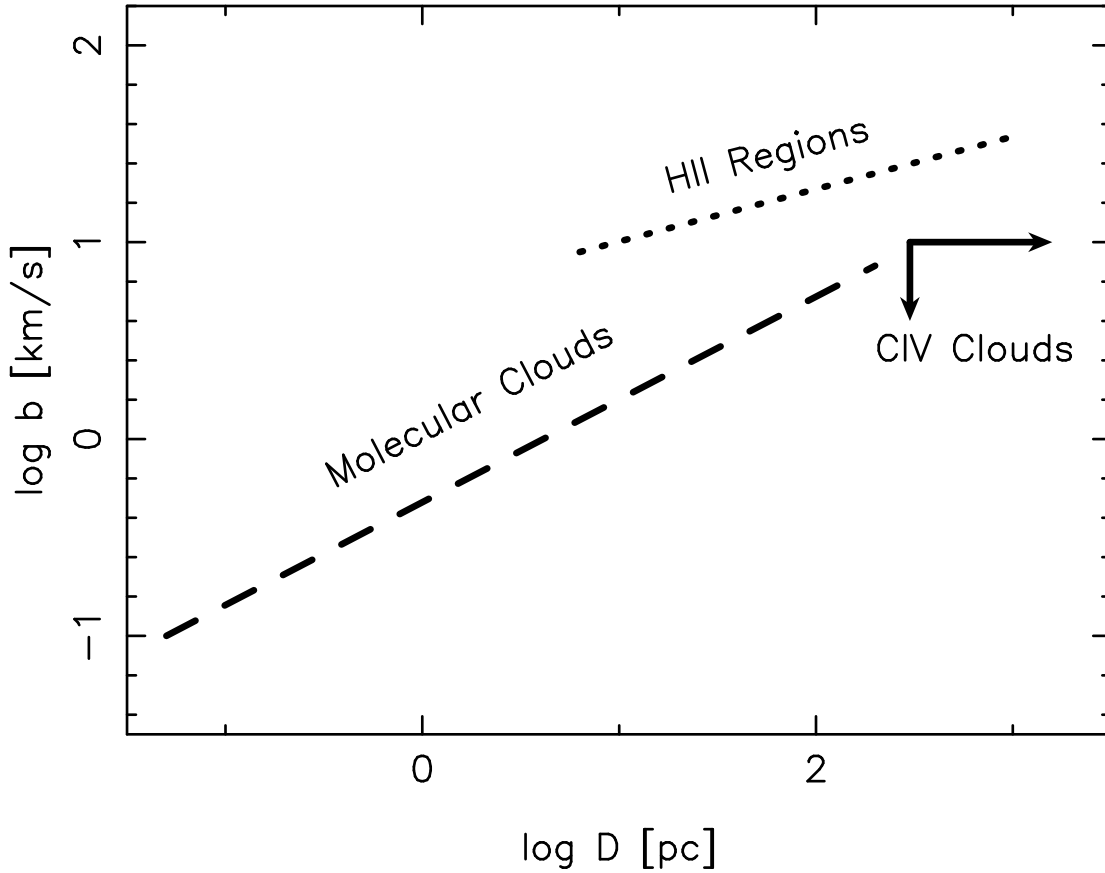


Fig. 16.— The plot shows the relation between the turbulent Doppler parameter  $b$  and the size  $D$  for molecular clouds and HII regions. The solid curves schematically represent a compilation of data points from O’Dell (1991)). The two arrows corresponds to the upper limits on turbulent line widths of individual CIV components and the lower limits on CIV cloud sizes corresponding to a 50% difference in column density. CIV systems are more quiescent for their size than HII regions.